Title
Nanoscale Optical Devices: Force, Torque and Modulator

Author
Liu, Ming

Publication Date
2010

Peer reviewed|Thesis/dissertation

Nanoscale Optical Devices: Force, Torque and Modulator

By

Ming Liu

A dissertation submitted in partial satisfaction of the requirements for the degree of

Doctor of Philosophy

in

Applied Physics

in the

Graduate Division

of the

University of California, Berkeley

Committee in charge:

Professor Xiang Zhang, chair
Professor Ming C. Wu
Professor Yuen-Ron Shen

Fall 2010

Abstract

Nanoscale Optical Devices: Force, Torque and Modulator

by

Ming Liu

Doctor of Philosophy in Applied Physics

University of California, Berkeley

Professor Xiang Zhang, Chair

Manipulating and utilizing light in nanoscale are becoming tasks of not only scientific interest, but also industrial importance. My research includes two major topics in nanoscale optics: 1. Nanoscale optical motor. 2. Optical modulator based on novel materials.

Light carries both linear and angular momentum, and therefore generating force or torque with light is feasible. The ability to provide torque in nano-meter scale opens up a new realm of applications in physics, biology and chemistry, ranging from DNA unfolding and sequencing, to active Nano-Electro-Mechanical Systems (NEMS). In the first part of this dissertation, I demonstrate a nano-scale plasmonic structure generating a significantly large rotational force when illuminated with linearly-polarized light. I show that a metallic particle with size of 1/10 of the wavelength is capable of rotating a silica microdisk, 4,000 times larger in volume. Furthermore, the rotation velocity and direction can be controlled by merely varying the wavelength of the incident light, thereby inducing different plasmonic modes which possess different torque directions. The tiny dimensions along with the tremendous torque may have a profound impact over a broad range of applications such as energy conversion, and in-vivo biological manipulation and detection.

Compared with the interaction between particles and photons, the optical force between particles is of fundamentally important as well. In the end of the first part, I propose a new technique to measure the optical binding forces between two plasmonic particles. By

using localization technique on a build-in cantilever, I prove the potential to measure the force with accuracy up to sub-pico-Newton.

The second part of this dissertation is about the modulation of light, an optical modulator. Integrated optical modulator with high modulation speed, small footprint and large optical bandwidth is poised to be the enabling device for on-chip optical interconnects. However, present devices suffer from intrinsic narrow-bandwidth aside from their sophisticated optical design, stringent fabrication, temperature tolerances and large foot print. By using graphene, a monolayer of carbon atoms, I experimentally demonstrated a broadband, high-speed, waveguide-integrated electroabsorption modulator. The extremely strong interaction between light and relativistic electrons in graphene allows us to integrate an optical modulator within an ultra-small footprint while operating at a high speed with broad bandwidth under ambient conditions. Even monolayer of being less than 1 nm in thickness, its modulation effectiveness is comparable with the best materials like Ge and SiGe with tens nanometers. In addition, the athermal optoelectronic properties of graphene make the device immune to harsh operation environments, in sharp contrast to all existing semiconductor approaches.

Table and Contents

Table and Contents

Chapter 1

Introduction of Nano-scale Plasmonic Light-mill

This dissertation deals with the potentials of two devices: a nano-scale optical light-mill and a fast graphene-based optical modulator. In this chapter, an overview of optical motors is presented.

Light-mill, as the name implies, is a device that transforms energy directly from light into mechanical movements. As the by-product of some chemical research, it was first invented by chemist Sir William Crookes[1], whose name was later used to name the equipment as Crookes radiometer. The light-mill excited broad interests and intense discussions a century ago, because it was believed to be the first direct observation of momentum carried by photons, which was predicted by Maxwell's equation. Although later it was proved by Reynolds that the torque on the radiometer was actually caused by thermal transpiration[3], researchers continued to search for ways to utilize the momentum of photons and to use it to generate forces.

Nano-scale plasmonic light-mill, which shares a similar four-vaned structure as traditional light-mill, is the approach I use to generate torque from light. Despite of the similarity of the structure, this device works under different mechanisms as its traditional analog. Instead of using temperature gradient, it utilizes the angular momentum carried by photons. Before going into the details of the device design, I will first discuss the background of optical forces and some recent progresses in plasmon-enhanced forces.

1.1 Optical Force

As early as 1619, Kepler announced his belief that light carried momentum, owing to the fact that comet tails always point away from the sun. In his theory, the comet tails felt the pressure from sunlight. Ever since then, in the following four centuries, numberless physicists, including Newton and Einstein, have devoted into understanding the origin of the momentum. And even now, there are still debates in this field[4].

After Kepler's proof was later proved to be induced by solar wind but not light pressure, another famous trial was then carried out in 1873, when Sir William Crookes invented a

radiometer, and with which he believed that he had found the true radiation pressure[1]. Again this pressure, which was actually 100,000 times larger than theoretical prediction, was proved to be due to the thermal effect on the vanes.

The true measurements of electromagnetic radiation pressure in a vacuum were individually demonstrated by Lebedew[5], and by Nichols and Hull[6,7], in 1901. By using apparatuses which were very similar with Cavendish's experiment, they confirmed the existence of momentum carried by light. Although it has been widely accepted now that photons possess momenta, the correct form of energy-momentum tensor, and therefore the magnitude of momentum carried by each photon in a dielectric medium, have been debated for about a century[4].

The optical force has a far-reaching and important impact in the past two decades. It has been at the core position of a revolution in the interaction between light and atomic systems, which includes topics like laser cooling[8,9] and Bose-Einstein condensation(BEC)[10]. Optical forces can work on not only atoms, but also macroscopic particles, notably through optical trapping where light can readily trap and manipulate dielectric particles without damages[11].

With the increase of computing ability, many methods have been developed in the past years to simulate the optical force. Here I briefly introduce three of them. The first one is based on discrete dipole approximation (DDA). DDA is a method that is widely used for computing the scattering of radiation by arbitrary particles. It divides the particle into small pieces, which can be regarded as dipoles for approximation. Because the responses of each dipole under the influence of the incoming wave and their neighbors can be analytically given by Mie theory, the total response can therefore be simulated. After obtaining the electrical and magnetic field distributions, one can calculate the total optical force by integrating the force on each dipole, which can be given by

$$\vec{F} = p_j \vec{\nabla} E_j \tag{1.1}$$

Then the time-averaged force on a particle with volume V is given by:

$$\vec{F} = \frac{1}{4}\int P_j \vec{\nabla} E_j^* dV + c.c. \tag{1.2}$$

Another method to calculate the optical force, especially forces between coupled particles, is based on the principle of virtual work. From the frequency drift due to coupling, the force can be derived as[12]:

$$F = -\frac{1}{\omega}\frac{d\omega}{d\xi}U = -\frac{1}{\omega_0 + \Delta\omega}\frac{d(\omega_0 + \Delta\omega)}{d\xi}U \approx -\frac{1}{\omega_0}\frac{d\Delta\omega}{d\xi}U \tag{1.3}$$

Here U is the total electromagnetic energy, and ω_0 is the eigenfrequency of the arbitrary particle.

The third method, maybe also the most widely used one, is the Maxwell's stress tensor. This second rank tensor provides a convenient way to calculate the force acting on a particle by only evaluating the integral of stress tensor on the surfaces. The stress tensor T can be given by:

$$T_{ij} = \frac{1}{4\pi}(E_i E_j + H_i H_j - \frac{1}{2}(E^2 + H^2)\delta_{ij}) \tag{1.4}$$

Here E and H are electric and magnetic field distribution of the electromagnetic wave, and δ_{ij} is Kronecker's delta. With the development of computational electrodynamics modeling techniques, for instance finite-difference time-domain (FDTD) method and finite element analysis (FEA), larger and more complex systems can be now simulated, and the optical force on them can be evaluated in this way.

In my work I used both the first and the third methods to calculate the force on the light-mill. Details will be discussed in the following chapters.

1.2 Optical Tweezers

Optical forces have many profound applications, among which are optical tweezers. It has been over twenty years since the invention of optical tweezers, which are now the most popular form of optical micromanipulation. This method is versatile and simple: only a laser beam and a high numerical aperture (NA) objective lens are needed. And the only requirement to the sample is its refractive index being larger than that of the solution. While with the help of optical tweezers, researchers can launch studies more than only manipulating a cell or a particle. It also makes it possible to investigate the mechanical properties of proteins, wind and unwind DNAs, or fabricate photonic crystals, listing just a few.

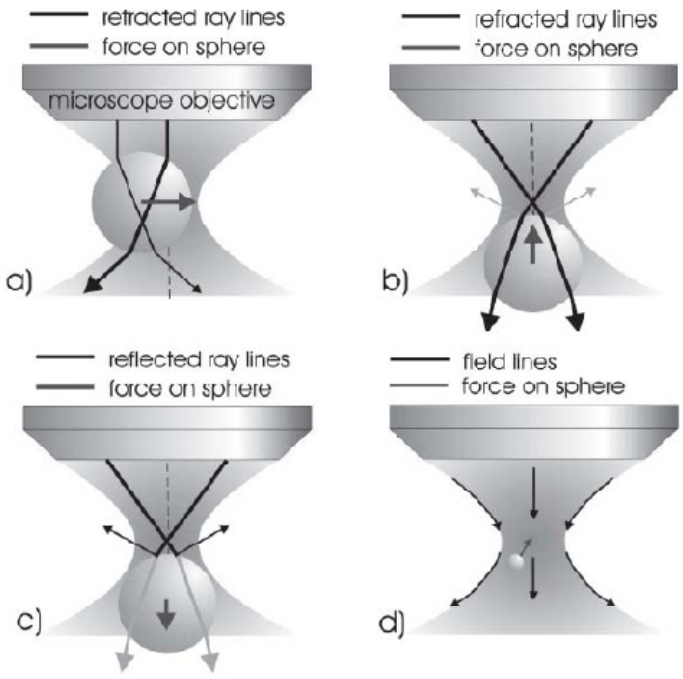

Figure 1.1 Schematic illustration of optical tweezers[13]. A strongly focused light beam is used to trap the particle. The intensity gradient draws the particle towards the focus point, while the radiation pressure, owing to the scattering of photons by the particle, pushes it along the propagating direction of the light. For a transparent particle, the trapping force can be understood by ray optics. When a particle is at the edge of a Gaussian beam, as shown in a), larger portion of light (thicker black line) are refracted away from the part which is closer to the center of the beam. The sum of the force will draw the particle towards the axis of the beam. When the particle is offset from the focus plane along the axis, the sum of the force will drag the particle upwards. As a consequence of that, the particle will stay stable along z-direction near the focus point. For the optical trapping, there is always a competing between the optical trapping force and the repelling forcing due to scatterings. This additional effect of radiation pressure will disturb the trapping system, and to overcome this, a high NA microscopy objective lens is needed. For particles smaller than the wavelength, its polarisability is more important than the transparency. In the quasi-static field approximation, the electric-filed-induced dipole aligns to the gradient of the electric field, known as the Ponderomotive force.

Chapter 1 Introduction

The conventional optical tweezers are shown in Figure 1.1. To achieve a beam spot that is tight focused to diffraction limited at the focus plan, a high NA microscope objective lens with high magnification is generally used. High NA objective lens ensures that the beam can be confined in three dimensions, both lateral and axial directions. Therefore the gradient is also three dimensional. Since the narrowest focused spot after the objective lens has a diameter $D \simeq \frac{2\lambda_0}{\pi \cdot NA}$, the traditional optical tweezers cannot achieve subwavelength confinement.

The trapping process of a dielectric particle can be understood by ray optics. When the particle randomly moves close to a focused Gaussian beam, its closer edge to the axis of the beam will refract larger portion of light. This refraction will generate a force, which draws the particle towards the axis. As a result of that, the particle will be localized in the x-y plane. If the particle is offset along the axis in the z direction, owing to Brownian motion or other reasons, the sum of the optical force will drag it back, as shown in Figure 1.1 b. Overall, we may see that the gradient of light intensity both in the lateral plane and along the propagation direction of the light are equally important in trapping a particle.

Another key point in trapping is the balance between the gradient force and scattering force. Gradient force induces trapping effect, however the scattering force tends to propel the particles away. The interplay between gradient force and scattering force dictates the exact equilibrium position for the trapped particle. Since the scattering force is only along the propagation direction of the light, the trapping force along z direction, or in the other word the intensity gradient along z direction, is extremely important in trapping. This is the reason for the widely use of high NA objective lens.

Optical trapping can trap not only large dielectric particles, but also small particles which is even smaller than the diffraction limit. In this Rayleigh regime, it is the polarisability of the particle, rather than the transparency, which is more important for trapping. The induced polarization on the particle tends to minimize its potential energy in the potential well created by light gradient. When the optical potential is lower than $-3k_BT$, where k_B is the Boltzmann constant and T is the local temperature, the particle can be considered to be trapped by the light.

To the induced dipole, the optical force always points towards the gradient direction, which means from the weaker intensity region to the stronger intensity region. However to a charged particle, the direction is reversed. A charged particle can also feel a nonlinear force in an inhomogeneous oscillating electromagnetic field, which is called Ponderomotive force[14] and can be written by

$$\boldsymbol{F_P} = -\frac{e^2}{4m\omega^2}\nabla E^2$$

Here m is the mass of the particle, and ω is the frequency of the electromagnetic wave. This nonlinear force plays a very important role in nonlinear processes, such as high-order harmonic generations[15].

A frequently asked question is why optical tweezers play such an important role in biologic researches, especially in elucidating the motion of molecules. Figure 1.2 shows how the optical tweezers work with molecules. Before measuring the molecules, the properties of the optical tweezers should be firstly evaluated. This can be done by studying the random Brownian motion of the trapped particle. We know that the kinetic energy of a free particle is in the order of k_BT along each dimension. In a harmonic potential well, this means the height a particle can reach. For a harmonic potential well, usually up to a few hundreds of nanometers, the restoring force can be considered to be linear. Therefore the motion of a trapped particle, with a mass m, inside a liquid with viscosity μ can be expressed by Einstein-Ornstein-Uhlenbeck theory with a Langevin equation:

$$m\frac{\partial^2 x}{\partial t^2} + \gamma\frac{\partial x}{\partial t} + \kappa x = (2k_BT\gamma)^{1/2}\eta(t)$$

Here $(2k_BT\gamma)^{1/2}\eta(t)$ represents the Brownian motions at the temperature T, with $\eta(t)$ standing for the stochastic process of motions as a function of time t. γ is the Stokes' drag term. For a particle with radius a, $\gamma = 6\pi a\rho v$. This Stokes' drag term can be considered as a strong damping to the oscillation equation, especially to high frequency vibrations. By measuring the roll-off frequency, which is usually below 1 kHz as shown in the top left panel in Figure 1.2, we can calculate the stiffness κ of the potential well, which may differ for different particles and incident light intensities.

After the optical tweezers is calibrated, the trapped particle can be used as a very sensitive force transducer or a "handle". It opens a new era of research in single molecule studies. Before the invention of optical tweezers in 1980s, researchers can only learn the bulk properties of molecules, or their performance in bulk biological samples. As a true revolution, optical tweezers make it possible to carry out those studies in the molecule level. Although the trapped particle could be still hundreds or even thousands times larger than the molecules in size, its accurate measurement in displacement allows it to be used in evaluating the mechanical properties on the level of single molecule.

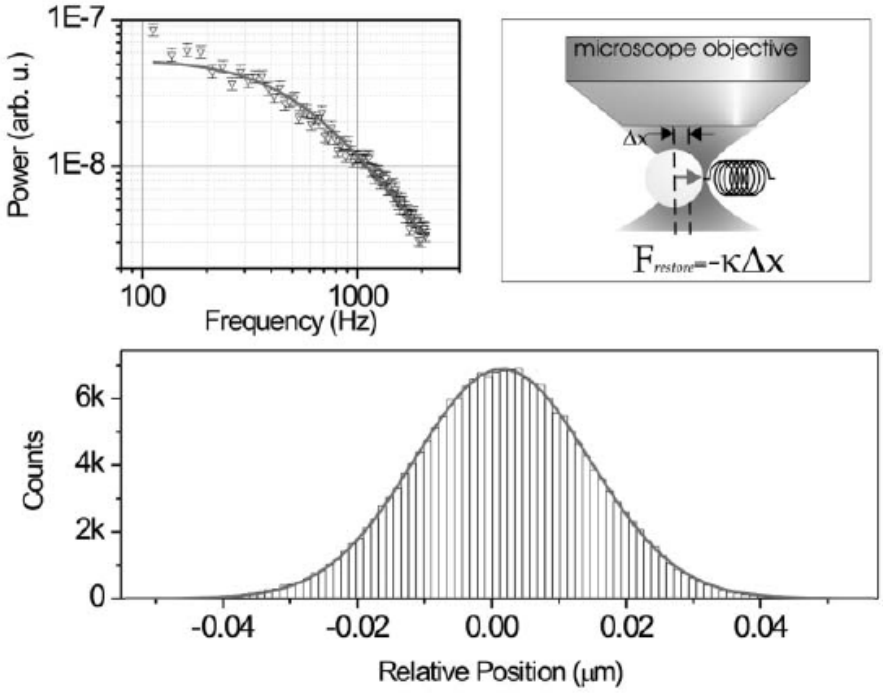

Figure 1.2 Calibration of optical tweezers[13]. Before using the optical tweezers to measure the stiffness of molecules, it is very important to calibrate the performance of the optical tweezers. To study molecules, usually optical tweezers are not used to trap them directly, but trap a dielectric particle which is larger than the diffraction limit. And the molecules are attached on the particle, with the other end fixed on the substrate.

A trapped bead can be considered as a very sensitive force transducer. It is because that the particle can be treated as a Brownian particle in a harmonic potential, with the random motion being restrained by the restoring force of optical trapping. Therefore by measuring the fluctuations of the beads, as shown in the top left panel, the stiffness of the optical potential well can be evaluated. The bottom panel shows the histogram of the center positions of the Gaussian distribution. By using a quadrant photodiode (QPD), the three dimensional positions of the particle can be mapped. By connecting the particle to a molecule, with the other end of the molecule fixed, the stiffness of the molecule can be evaluated.

When a particle is used as a "handle", the optical tweezers need not to trap the molecule directly, which may avoid potential thermal damages and also be practically easier since the molecule itself is difficult to be trapped because of the tiny volume. By imaging the trapped particle to a quadrant photodiode, its position can be monitored accurately. Then with suitable surface chemical modifications, the molecules can be attached to the particles. Those molecules usually form mono-layer on the surface of the particle. Researchers can then move the particle close to a substrate, and attach the other ends of the molecule on the substrate. With only one molecule attached on the substrate, which usually means a lot of trials, the stiffness of the molecule can then be measured.

The key technique in the optical tweezers is locating the position of the particle. There could be other methods to monitor the position of the particle. For instance, instead of using a quadrant photodiode, by using a charge-coupled device (CCD) one may find the center of a bright spot by fitting its image to a 2 dimensional Gaussian distribution. In one of the following chapters, I will introduce a new device based on this technique, where I use cantilevers to measure the optical forces between plasmonic particles.

1.3 Optical Torque

Photon carries not only linear momentum, but also another characteristic – angular momentum which is independent of its frequency. Both of them can be used to generate torque on an object. In this section I will brief introduce the background and research status for spin/orbital angular momentum and the devices based on them.

It has been even written in the high school textbooks that light has polarizations, and a complete coordinate set of them are left circular polarization and right circular polarization. It has also been proven that the circular polarized light carries angular momentum $\pm\hbar$ for different circular polarizations. When photons interact with other materials, the angular momentum can be transferred between them, with the total angular momentum of the system conserved, a similar process as the transfer of linear momentum.

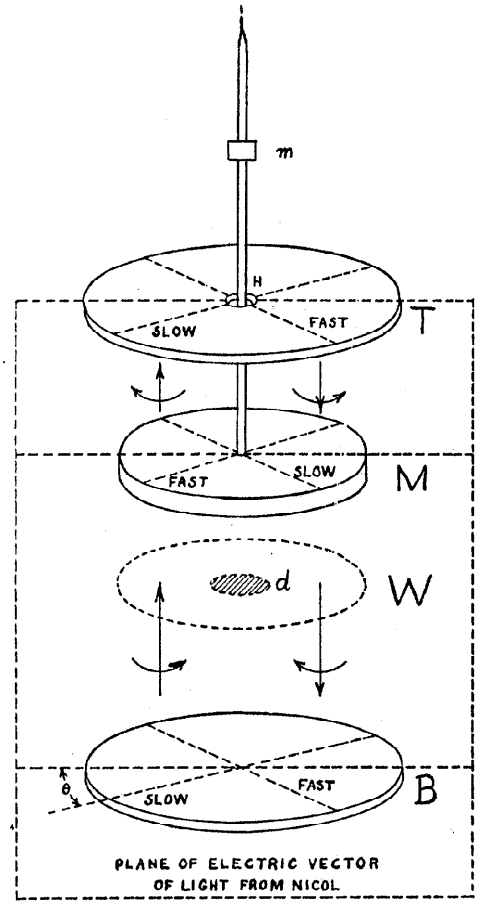

Figure 1.3 Schematic illustration of measuring the spin angular momentum of light[16]. A wave plate can change the polarization status of the light, and therefore change the angular momentum carried by it. As a consequence of angular momentum conservation, the wave plate received an impetus, which was the same magnitude but opposite directions as the changes of the light. This impetus twisted the wave plate-string system and the magnitude of the impetus, or torque, can be evaluated by the rotate angle of the wave plate. (θ in the figure.)

As early as in 1936, the angular momentum of light has been experimentally proved by Beth[16], using a similar setup as previous experiments in measuring the linear momentum[5-7]. In his experiment, as schematically illustrated in Figure 1.3, a wave plate

was used to change the polarization status of an incident beam of light. Therefore the (spin) angular momentum of the light was also changed. As a consequence of angular momentum conservation of the system (including light and wave plate), the wave plate received impetus which was the same magnitude but opposite directions as the change of angular momentum carried by light. This impetus induced rotation of the wave plate, and its magnitude could be calculated by measuring the rotate angle.

After the confirmation of the angular momentum carried by circular polarized light, it had been a long time for researchers to take it for granted that the only form of angular momentum carried by light is spin. And it was until 1992 when Allen et al.[17] theoretically predicted that Laguerre—Gaussian beam possess an orbital angular momentum of $l\hbar$ per photon, as the beam's complex field amplitude can be given by:[18]

$$u_{pl}(r,\phi,z) \propto \frac{z_R}{(z_R^2+z^2)}\left(\frac{r^{1/2}}{w(z)}\right)^l L_p^l\left(\frac{2r^2}{w^2(z)}\right)\exp\left(-\frac{r^2}{w^2(z)}\right) \times \exp\left(\frac{-ikr^2 z}{2(z_R^2+z^2)}\right)\exp(-il\phi)\exp\left(i(2p+l+1)\tan^{-1}\frac{z}{z_R}\right) \tag{1.5}$$

Here w is the waist size of the beam, and $L_p^l\left(\frac{2r^2}{w^2}\right)$ stands for the associated Laguerre polynomial, with p the radial mode index and l the azimuthal mode index. z_R is the Rayleigh range. So it can be seen that in additional to the azimuthal mode index l, there is another parameter p. This parameter describes the node numbers in radial direction.

The beam which satisfies Laguerre—Gaussian equation is structurally stable with propagation, although in the center of the beam there is a singular point for phase. Upon going around this singular point within a plane perpendicular to the propagation direction, the phase of the beam increases/decreases $2\pi l$ for a complete circle. Another viewpoint for this special type of phase is to look at the phase front. A helix phase front defers this mode from other types of beams. Figure 1.4 shows the phase front of a Laguerre—Gaussian mode with an azimuthal mode index l=3. The phase repeats its shape after every period λ, but only rotates fully after $l\lambda$. The insets in Figure 1.4 a shows the intensity of the interference pattern between the Laguerre—Gaussian mode and a plane wave. Figure 1.4 b shows the similar interference patterns with l=2 and 3.

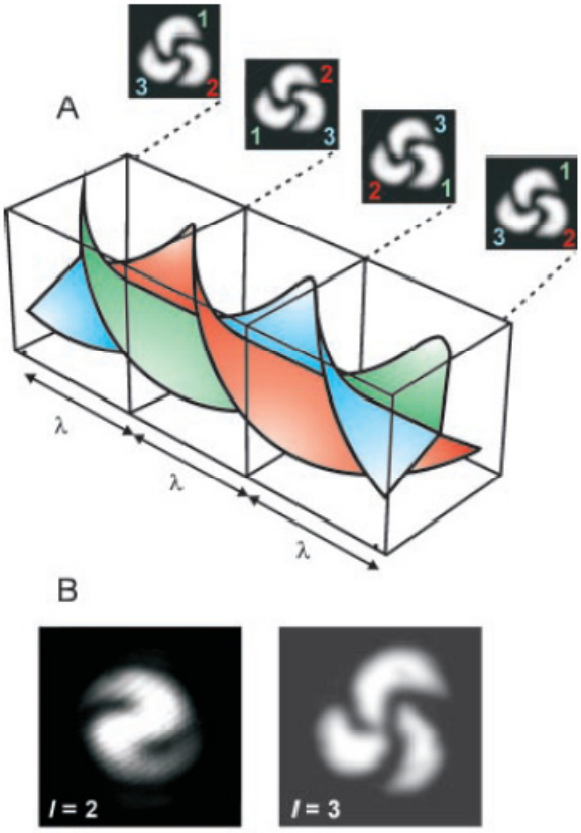

Figure 1.4 The phase front of Laguerre—Gaussian mode[19]. For the mode shown in **A**, the azimuthal mode index *l* =3. That means the phase increases/decreases 6π when follow a path around the beam axis and within a plane perpendicular to the propagation direction. At the axis position, the phase has a singular point. The phase front of the mode forms a helix shape. Although this shape repeats itself after propagating λ, it fully overlaps with itself only after 3λ. The interference between this mode and a plane wave is shown in the insets. B shows the interference patterns between a plane wave and Laguerre-Gaussian modes, with *l*=2 and *l*=3 respectively.

The angular momentum carried by a light beam can be investigated by looking at the linear momentum of light. With the complex amplitude of the electromagnetic field written as $u = u(r, \phi, z)$, where r, ϕ, z are the radial, azimuthal and longituidinal coordinates, the linear momentum can be written as:[17]

$$
\begin{aligned}
p &= \frac{\varepsilon_0}{2}(E^* \times B + E \times B^*) \\
&= i\omega\frac{\varepsilon_0}{2}(u^*\nabla u - u\nabla u^*) + \omega k\varepsilon_0 |u|^2 \hat{z} \\
&+ \omega\sigma\frac{\varepsilon_0}{2}\frac{\partial |u|^2}{\partial r}\hat{\phi}
\end{aligned}
\tag{1.6}
$$

Here the paraxial approximation is considered. $\hat{z}$ and $\hat{\phi}$ are unit vectors along longitudinal and azimuthal directions. σ equals to ± 1 for left and right circular polarizations, respectively.

The angular momentum of the light, which can be considered as the cross-multiplication between displacement and linear angular momentum, $r \times p$, is not zero along the propagation direction $\hat{z}$ when the first or third (azimuthal) term in eq. 1.6 is not zero. The azimuthal term gives the spin angular momentum, while the first term is associated with orbital angular momentum. For circular polarized light, eq. 1.6 is non-zero because σ equals to ± 1. The in-plane phase changes in a Laguerre-Gaussian beam contribute to the first term in eq. 1.6. This is the mathematical origin of the orbital angular momentum carried by a Laguerre-Gaussian beam.

Applications utilizing optical torque

Modern motors highly rely on gears, as which can transmit the powers and produce mechanical advantages through gear ratios. Therefore, linear motions are usually transformed to rotational motions for a broader category of applications.

Same here in optical manipulations. Trapping a particle and moving it provide three degree of freedoms, while rotating the particle can provide three more. The ability to rotate a particle can have important applications in biology, such as DNA winding and unwinding[20], particle sorting, and fluids mixing[21]. It is also very promising for harvesting solar energy, and driving Microelectromechanical systems (MEMS).

The first experiment using optical tweezers to rotate a particle was carried out in 1995 by He, et al[22]. In his experiment, a Laguerre-Gaussian beam is used to trap an absorptive particle, black high-Tc superconductor ceramic powder in his case. By absorbing the photons which carry angular momentum, the particle was rotated in solution. Absorbing the photons of course is a direct way to transfer angular momentum to the particle, but it also may introduce several severe problems, which limit its use. Firstly, photons carry not

only momentum. Actually the majority part associated with photon is its energy, whose relation with the momentum can be given by $E = pc$, where c is the velocity of light in vacuum. When photons are absorbed by a particle, their energies are transformed into heat and the temperature of the system is therefore increased. This thermal effect definitely limits its application in bio system where temperature effect is critical. The second shortcoming is related to the optical scattering. By absorbing photons, the particle obtains not only the angular momentum, but also the linear part, which tends to push the particle away from the focus point. Both of these two points prevent the absorbing scheme from practice.

To find a technique which can reduce both the thermal effect and scattering effect but keep the magnitude of the torque is hence critical to turn it from purely scientific research into real applications. The breakthrough was carried out by an Australia group in 1998[23]. They smashed birefringent material, calcite in their experiment, into micron-meter size, and used it as a tiny wave plate to change the polarization state of an elliptical polarized light. The calcite particle is almost transparent and in this way they avoided the thermal effect owing to absorption and also made the particle much easier to be trapped due to the weak scattering force. However this technique is directly limited by the choices of the materials. Since the birefringent effect is weak for most materials, there are only a few candidates available. To keep the birefringent property, the materials need to be single crystallized, which also restricts the fabrication methods. Moreover the polarization state of the incident light needs to be carefully tuned to maximize the torque, which means a quarter wavelength wave plate and half wave plate are needed other than only a simple Gaussian beam. Therefore there are only a few researches along this direction after the first publication.

If we compare the experiments utilizing spin angular momentum and those utilizing orbital angular momentum, one obvious difference is the trace of the trapped particles. For a particle rotated by light carrying spin angular momentum, it tends to rotate regarding to itself, as shown in the first column in Figure 1.5[24]. On the other hand, if the photons carry orbital angular momentum, the particle tens to rotate around the axis of the light beam. This is because that the rotational optical force is generated by the gradient of the phase, which is along the azimuthal direction since the phase is changing in plane. The trace of this case is shown as the larger yellow arrow in the top panel in Figure 1.5. The magnitude of the torque generated by either spin or orbital can be evaluated from the rotation speed times the viscosity of the solution.

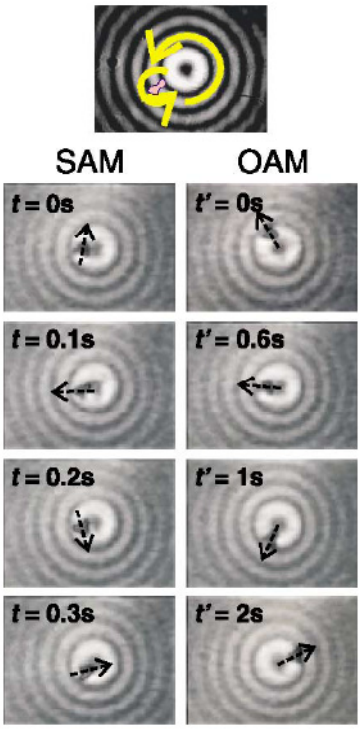

Figure 1.5 Comparison between particles rotated by spin angular momentum and orbital angular momentum[24]. Multi-ring pattern of the light was owing to the imperfection of the Gaussian beam. In the left column, the incident light was a circular polarized light. When it is absorbed by the particle, its spin angular momentum was delivered to the particle and induced rotation with the rotation axis being the topological center of particle. However to a particle driven by Laguerre-Gaussian beam, the particle tends to rotate around the axis of the beam, indicating that the rotational force is due to the gradient of the phase and directs along the azimuthal direction.

Both of the two schemes introduced above have their disadvantages such as special requirements to the material choices, optical designs to generate Laguerre-Gaussian beam or specific elliptical polarizations, and lack of control methods. A third scheme based on MEMS fabrications has recently excited a lot of interests together with the fast development of nano-scale fabrication technology.

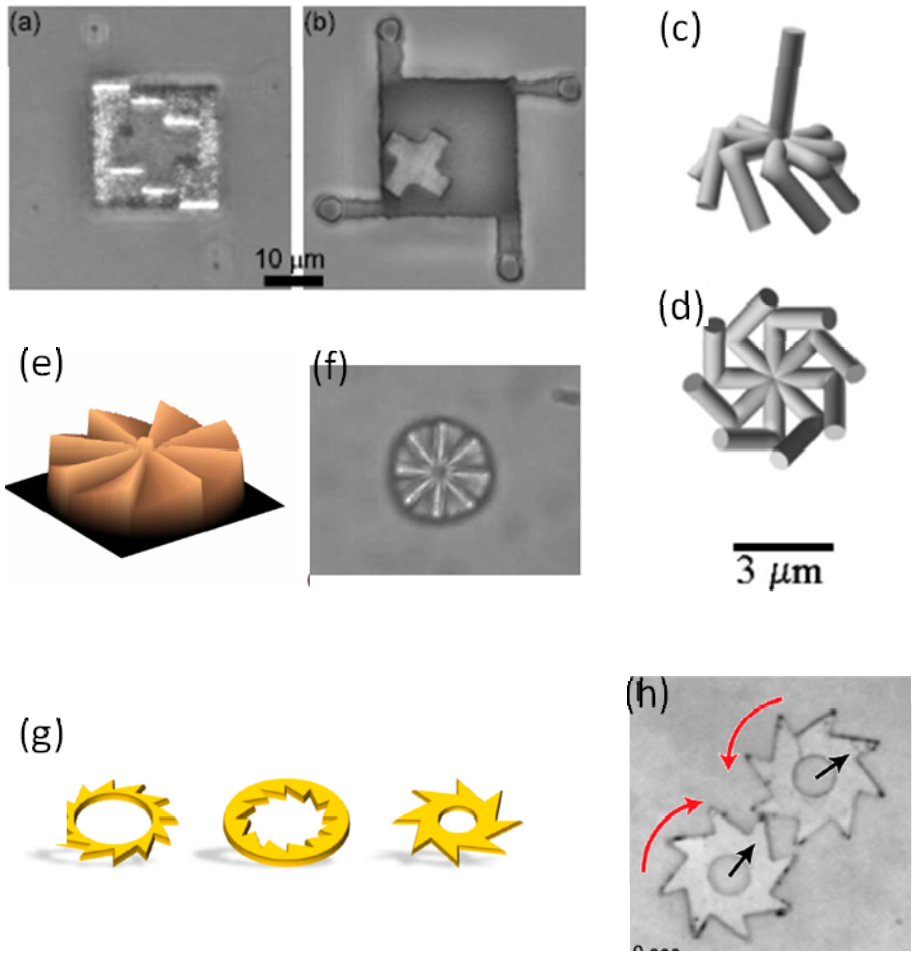

Figure 1.6 Different designs of MEMS motors[21,25-27]. With the broken in-plane symmetry, some of the particle scattered light in a similar manner as the windmill scattering wind flow (**a-d**)[21,25], or add various phase to the light (**e,f**)[26]. These particles are usually fabricated by optical lithography, and transparent materials are chosen to reduce thermal effect and scattering force. In some researches, the pump power of the incident laser can be as high as 100 mW, and the torque generated is sufficient to rotate the particle at 1000 rpm. One need be careful since this asymmetrical structure may also be driven by other mechanism, such as Brownian motion of bacteria (**g, h**) [27]or even water molecule, although this shape in **g** is also used to generate optical torque.

This third scheme utilizes directional refraction/reflection of light on a special shape which is usually micron-meter scale. Figure 1.6 shows some examples of the MEMS devices[21,25,26,28]. By breaking the in-plane symmetry, the particles scatter light at certain directions. As a consequence of that, they gain the optical torque. Modern fabrication techniques allow researchers to prepare those particles with transparent materials, which can reduce thermal effect and scattering optical forces, both of which are related to the optical loss of the materials. Those devices share similar shapes as Brownian motors[29], which use the fluctuation in random motions as the pump. Although at micron meter scale the Brownian motor effect can be orders smaller than the optical torque, its influence needs to be carefully considered when the motor goes small.

All the three schemes above need the particles to be at least several microns to accumulate strong enough torque. This originates from the weak dielectric-light interaction, and limits their applications in biology and NEMS. Therefore shrinking the size of the motor without losing its power is not only scientifically interesting, but also practically important. Plasmonic effect may provide a solution to this challenge.

1.4 Fundamental of Plasmonics

Plasmonic has been a rapidly increasing interdisciplinary research area in recent years. It provides the possibility to achieve novel optical properties such as negative permittivity and permeability through modifying the collective electron density oscillations coupled to the incident electromagnetic waves[30,31]. Many applications have been developed by using plasmonic effect, such as super lens[32], SERS[33], and metamaterials[34], to name a few. In this section, the fundamentals and applications of plasmonics will be explained.

1.4.1 Surface Plasmon Polaritons

Probably the most widely studied subject in plasmonics is surface plasmon polaritons. Being the collective oscillation of electrons at the interface between metal and dielectric, surface plasmon possesses several advantages compared with propagating electromagnetic wave in free space, such as shorter wavelength and stronger electric field. The behavior of surface plasmon at interface can be obtained by solving Maxwell's equations, including consideration of boundary conditions. Figure 1.7 shows the schematic illustration of the surface plasmon. We assume that the interface is between a dielectric media with positive permittivity ε_d at $x > 0$, and a metal with frequency-dependent complex permittivity $\varepsilon_m = \varepsilon_m' + i\varepsilon_m''$ at $x < 0$, with ε_m' being negative. The

solution is a surface wave, propagating along z direction with both electric and magnetic fields exponentially decay along $\pm\hat{x}$ directions.

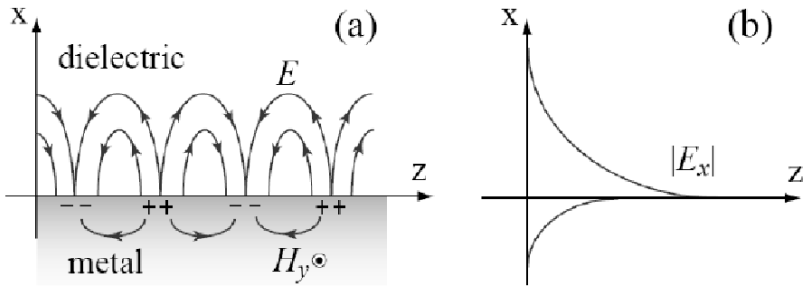

Figure 1.7 Surface plasmon polaritons formed at the interface between dielectric and metal. The collective charge oscillations excited by external electromagnetic wave form the transverse magnetic (TM) propagating wave. The *k*-vector of surface plasmon wave is larger than the k_0 in free space, therefore the *k* along x direction is imaginary, which leads to the exponentially decay for both electric and magnetic fields, as shown in **(b)**. In the free space, this decay length is usually on the order of a few hundred of nanometers, while inside metal it is about tens of nanometers.

By solving the Maxwell's equations with boundary conditions included, one may get the dispersion curve for the surface plasmon which can be written by:

$$k_{sp} = k_z = k_0 \sqrt{\frac{\varepsilon_m \varepsilon_d}{\varepsilon_m + \varepsilon_d}} \tag{1.7}$$

Here $k_0 = \frac{\omega}{c}$ is the wave vector in free space. ε_m, the permittivity of the metal, is a function of frequency, which can be given by Drude model:

$$\varepsilon_m(\omega) = \varepsilon_\infty - \frac{\omega_p^2}{\omega(\omega - i\gamma)} \tag{1.8}$$

Here ε_∞ is the permittivity at infinite large frequency, and can be considered as 1 for approximation. ω_p is the plasma frequency of the metal, and is proportional to the electron density *n* as shown by the equation:

$$\omega_p^2 = \frac{ne^2}{\varepsilon_0 m}$$

For noble metals, the frequency of ω_p is always at UV region, for instance $1.4\times10^{16} rad/s$, $1.5\times10^{16} rad/s$ and $2.2\times10^{16} rad/s$ for Au, Ag, and Al, respectively. γ in eq. 1.8 is the damping term due to the inelastic scattering between electrons, and it is always 2 to 3 orders smaller than ω_p for good conductors. For example, γ for Au, Ag, and Al are only $1\times10^{14} rad/s$, $8\times10^{13} rad/s$, and $1.1\times10^{15} rad/s$. The existence of γ gives the imaginary part of $\varepsilon_m(\omega)$, which gives the imaginary part to k_{sp} in eq. 1.7. Imaginary part of k_{sp} is related to the propagating length of the surface plasmon, which is usually in the order of tens of microns.

Since the permittivity of metal $\varepsilon_m(\omega)$ is a function of frequency, the ratio k_{sp}/k_0 is therefore also a function of frequency, as shown in Figure 1.8:

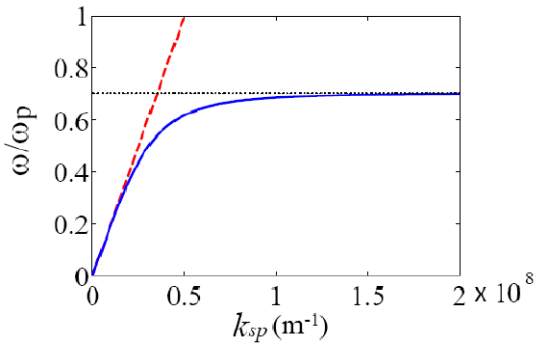

Figure 1.8 Dispersion curve of surface plasmon. Blue, the surface plasmon approaches the limit of $\omega_p/\sqrt{2}$. Red, the dispersion of light in the dielectric media.

1.4.2 Localized Surface Plasmons

The existence of surface plasmon does not require a flat metal surface. A curved surface such as sphere or cylinder can also support it. Such surface plasmon with three dimensional confinements is called localized surface plasmons. The frequency of a localized surface plasmon can also be analytically solved from Laplace's equations together with suitable boundary conditions. However to complex structures, the assistance from computer is required.

The localized surface plasmon always accompanies with electric field enhancement. Since the magnitude and resonance wavelength of the enhancement are related to the shape of the plasmonic structure and can be changed through fabrication designs, the study on localized surface plasmon has excited a lot of interests in recent years. The enhanced electric field in the electromagnetic wave can increase the efficiencies of many nonlinear processes, such as Raman process or laser emission.

Surface plasmon has attracted a lot of interests in interdisciplinary researches. For instance, merging plasmonics with quantum systems[35] provides challenges for both theory and experiment, coherent phenomenon in plasmonics provides novel line shapes[36], active plasmonic device and plasmonic laser beats diffraction limits[37], improved sensors can have better sensitivity with ultra-small size[38], new type of catalyst may boost researches in chemical reactions, and novel biological applications may improve diagnosis and treatment efficiencies[39].

1.5 Plasmonic Forces

Surface plasmon polaritons and localized surface plasmons have several advantages in optical trapping. Take a metallic tip for example[40]. Firstly, the tightly focused light on the metallic tip has highly confined evanescent wave which is beyond the diffraction limit and significantly reduce the trapping volume. Secondly, the large gradient of the evanescent wave enhances the trapping force. Thirdly, enhancement of the electromagnetic field allows a weaker illumination and reduces damages on the biological samples.

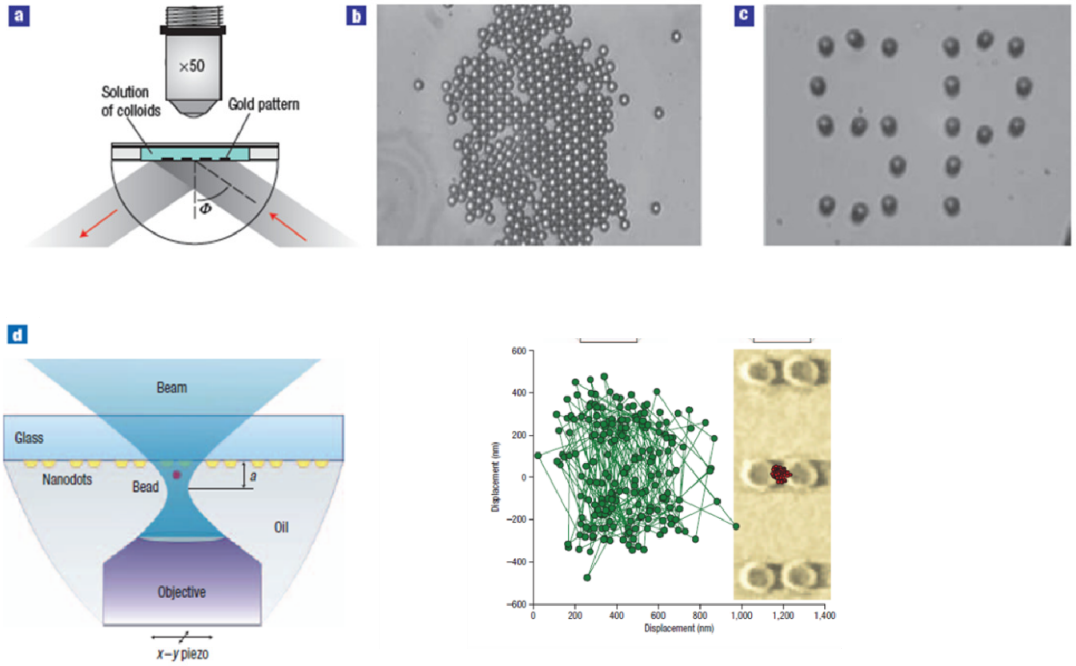

Figure 1.9 Nano-scale optical trapping enhanced by plasmonic resonance[41,42]. The plasmonic enhanced optical trapping have several advantages. (1), smaller trapping volume due to the gradient of the evanescent wave. (2), stronger trapping force due to the electromagnetic fields enhancement in plasmonic resonance. (3), weaker illumination required, which is safer for biological samples. Surface plasmon trapping also has obvious shortcoming, for instance it is hard to move the trapped particles.

Latest researches[41,42] have demonstrated that localized surface plasmon can be used to trap nano-scale particles, as shown in Figure 1.9. In the first experiment shown in 1.9 **a**, a parallel beam was used to excite the surface plasmon resonance on metallic disks. Although the parallel beam did not provided trapping force, the resonances on the disks generated gradient force and trapped dielectric particles. This trapping force can be further increased by designing the plasmonic structure to provide larger field gradient, such as in the gap of a plasmonic bow-tie (Figure 1.9 **d**).

Although plasmonic can dramatically improve the performance of the optical trapping, its disadvantages are also apparent. At the present stage, manipulating the trapped particles is still difficult because the plasmonic structures are usually fixed on the substrate. Finding a way to move the plasmonic tweezers is still an open question.

Plasmonics' high efficiencies in generating optical forces make them promising candidates for nano-scale motors which can be the locomotive force for NEMS devices. This will be studied in the following chapters of this dissertation.

1.6 Organization of the Dissertation

In this dissertation, I will separate my work to two parts. The first part is nano-scale plasmonic motor, and the second part is about a novel graphene-based waveguide-integrated broadband optical modulator, whose introduction will be included in chapter 5. The organization of the dissertation is as follows:

Chapter 1 is the introduction of optical force, and their applications including traditional optical tweezers, and novel plasmonic tweezers.

In chapter 2, I theoretically study a gammadion structure's optical properties, especially its capability to generate torque. I will study the influence from boundaries and environment, to get a full understanding of the origin of the torque.

In chapter 3, I propose the experiment setup, corresponding fabrication methods, and analysis the experiment results. Also I will discuss other influences in the experiment, such as temperatures and so on.

Chapter 4 will discuss a new technique based on localization method to measure the binding force between two plasmonic resonators.

Chapter 5 will discuss the first graphene-based optical modulator, which have less connection with the first 4 chapters. I give a brief review about graphene and modulators, by explaining the different working mechanisms for optical modulator and why graphene is a perfect material candidate for an electro-absorption modulator. Then I will propose a new configuration for the device, introduce the fabrication process, and do data analysis.

Finally, chapter 6 is the summary and perspective of my works including both plasmonic motor, and the optical modulator.

Chapter 2

Plasmonic Motor: Theory and Simulation

In this chapter, I will introduce one of the novel optical properties carried out by metamaterials: planar chirality. After discussing one special shape of the metamaterials, a gammadion structure, I will talk about the optical torque associated with its special optical responses, and also numerical methods to evaluate them.

2.1 Planar Chirality of Metamaterials

Chirality means that the object is not superposable with any of its mirror images. One generally recognized example of it is human hands. For a pair of hands, it is impossible to put one coincident with the other one, no matter how you orient the hands. Actually, the word chirality is originated from a Greek work for hand, and "handedness" is widely used in chemistry and physics to distinguish the chiralities.

The development of nano-scale fabrication technique allows researchers to create artificial "atoms" and "molecules", giving them symmetries which exist or even don't exist in nature, such as Mobius symmetry. Those "atoms" and "molecules" may possess unique responses to the electric or magnetic field of the incident light. Usually noble metals, such as Au, Ag, and Al, are used to form those artificial "atoms" and "molecules". Therefore the plasmonic resonance may enhance the unique optical properties, and generate a new research subject: meta-material.

Plasmonic structures with different shapes have been proposed and studied in the past two decades, and both negative permittivity and negative permeability have been achieved on metallic wires[43] and split rings[44]. For a metallic wire illuminated by light, the charge carriers, usually electrons in the metal, will be driven by the electric field of the light. Owing to the inertia of the electrons, their movements may have a phase delay compared to the incident wave. When this phase delay is larger than $\pi/2$, the overall polarization of the particle is negative, corresponding to a negative permittivity. By using similar concept, one can also achieve negative permeability with the resonance on split rings.

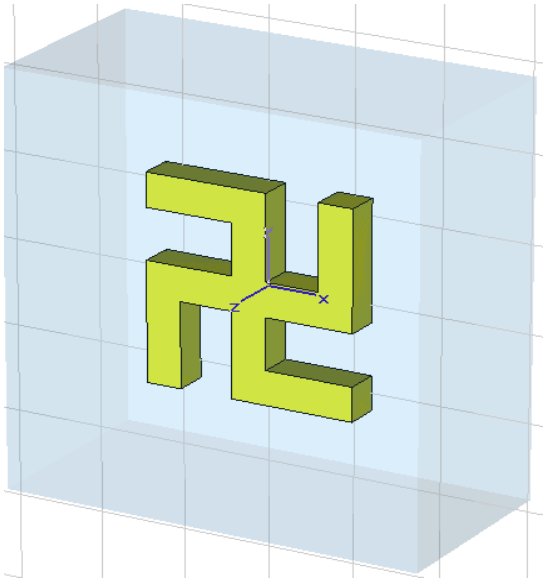

Figure 2.1 Schematic illustration of a gammadion-shape plasmonic lightmill. The size of the metamaterial unit can vary from centimeters to hundreds of nanometers, depending on the working frequencies required. Noble metals are usually used to reduce the intrinsic losses owing to the ohmic loss. The plasmonic structure can be considered as a tiny L-C circuit, and therefore its resonance frequency is reverse proportional to the footprint of the structure. The L-C analogy reveals that the structure can be stimulated by both the electric and magnetic field of the incident electromagnetic wave, for instance the E field along x or H field along z direction. Since the capacitance of the structure is proportional to the permittivity of the environment dielectric, the resonance frequency is also sensitive to the index of the surrounding media and can be used for sensing. Another advantage of the plasmonic resonance is the dramatically increased scattering area, which can be 10 times larger than the physical size of the plasmonic structure when at resonance.

In Figure 2.1 we show the schematic illustration of a plasmonic lightmill, which can be considered as the combination of four split rings, with 90 degree rotated from each other. We choose this four-fold symmetry because the two eigenfunctions (modes) for the two linear polarizations (ie, electric field along x or y direction and k along z direction in Figure 2.1) are identical. This guarantees that the particle won't be trapped along one

specific direction[45], or in other word the torque is independent of the incident light's polarization:

$$\tau(\theta) = \text{constant}$$

Plasmonic resonance always has an analogy to the traditional LC circuit[46,47]. The metallic wires form the inductor while the adjacent wires form the capacitor, whose magnitude can be influenced by the permittivity of the surrounding media. Therefore metamaterials can work from as low as gigahertz to hundreds of terahertz, depending on the demands. And their unit sizes may vary from centimeters to merely tens of nanometers, to meet the requirement. Since the resonance frequencies of the plasmonics are generally reverse proportional to the footprint of the plasmonic units, modern nanoscale fabrication techniques are usually needed to fulfill the task to push the resonance wavelengths to near-IR or even visible range. For instance, focused ion beam (FIB) and electron beam lithography (EBL) are common tools for this purpose.

The rapid development of computer science also allows us to carry out numerical simulations easily with commercialized softwares, such as CST microwave studio or COMSOL Multiphysics. Figure 2.2 shows the magnetic field and current distributions of the lightmill, by using a finite-difference time-domain method (FDTD). In the simulation, the linearly polarized incident light was set as plane wave, propagating along z direction with the electric field along x direction. Therefore the metallic wires on the top-left and bottom-right can be considered as forming a capacitor, which couples to the electric field of the incident light and transforms the energy from photon to plasmon. As a consequence of that, both magnetic field and current has maximum at the central region, and mathematically, their cross product is also maximized. As the incident light changes phase, the phases of magnetic field and current also change simultaneously. However, the cross product of them does not, which indicates that the Lorentz force will not change direction although the magnitude may change with time. This Lorentz force, the same origin as optical rectification, always accompanies with nonlinear processes such as second harmonic generation, which has already been demonstrated on split ring structures[48].

This uni-direction Lorentz force inspires me to study the optical force on plasmonic structures. And I choose lightmill because of its simple symmetry and rich physics which I will introduce in the following sections.

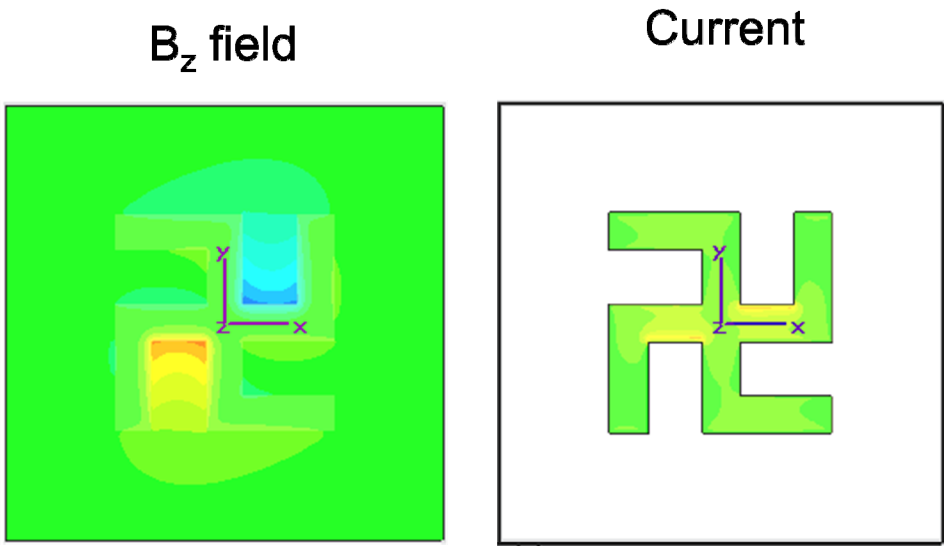

Figure 2.2 Numerical characterization of a lightmill. Left, z component distribution of magnetic field in the vicinity of the plasmonic structure. Right, current magnitude on the same structure. The incident light was set to be along z direction, normal to the plane of the sample, with linear polarization as electric field along x direction. In this case the plasmonic resonance is excited by the coupling between the capacitor and the electric field. It may also be excited by the coupling between magnetic field and the inductor. For instance when the light propagates along x direction with magnetic field along z direction, similar resonance pattern can be excited. For metamaterials, multiple modes can be supported, although here we show only the fundamental one of them. In the fundamental mode, current has maximum at the central region of the wires, and as a consequence of that, magnetic field is also maximized in the vicinity. Since the magnetic field and current change directions simultaneously, their cross product, which indicates part of the Lorentz force, will not change direction. That can also be considered as the optical rectification effect, which accompanies with second harmonic generation as has already been demonstrated by Wegener et al. This Lorentz force inspired us to propose this project.

2.2 Plasmonic Torque

As introduced in the first chapter, three different methods can be used to derive the optical force on the particle in the electromagnetic field. In this section, I use Lorentz force calculation to calculate the force, and the torque.

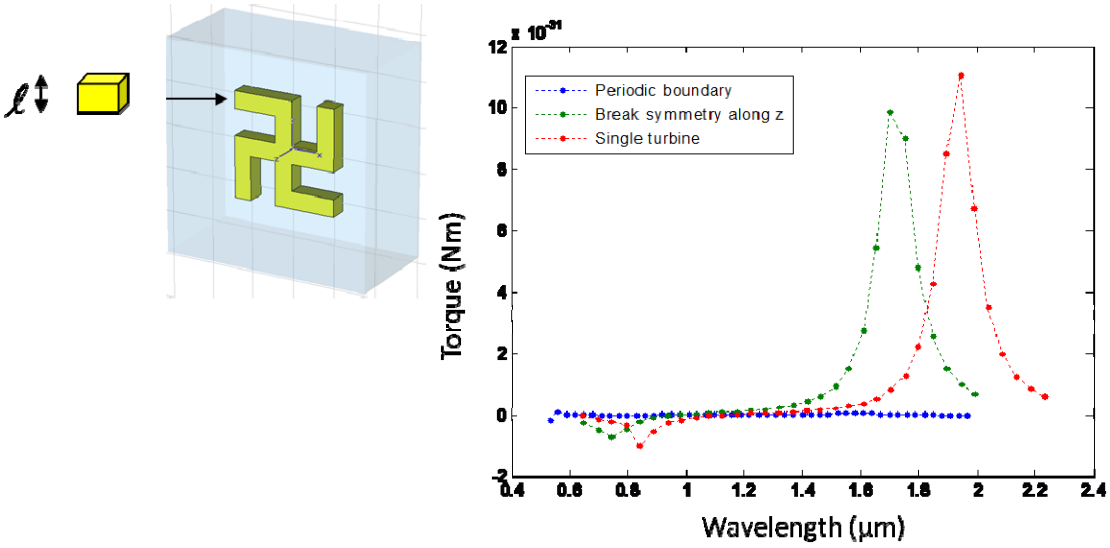

Figure 2.3 Optical torque calculated on the light mill. Left, schematic illustration of the Lorentz force integral. The lightmill, which is 200 nm in total length, and 40 nm in line width, is divided into mesh grid as small as 2 nm. Right, the simulated torques with different conditions. Red and blue are for open and periodic boundary condition respectively, with lightmill embedded in dielectric. Owing to the optical reciprocity, the periodical boundary condition, which corresponds to an infinite two-dimensional lattice, can not generate optical torque. The optical reciprocity can be broken by using different materials on the top and bottom of the lightmill, which is addressed in the green curve. In this case the optical torque can be generated. Both green and red curves contain two peaks, one sitting at 800 nm and the other sitting at 1800 nm. Those two peaks correspond to the two resonant modes supported by the structure. The interesting feature is that the torque changes signs for different modes, which indicates that the direction of the rotation can be controlled if we use this optical torque to drive a device.

To calculate the total optical torque on the plasmonic structure, we need first to consider the Lorentz force at different points of the lightmill. By dividing the lightmill into small mesh grids, with wide of the grids to be merely 2 nm, the Lorentz force on the grid can be expressed by:

$$\vec{F}(\vec{x})\cdot dx^3 = \vec{J}(\vec{x})\times\vec{B}(\vec{x})\cdot l^3 + (\nabla\cdot\varepsilon\vec{E}(\vec{x}))\vec{E}(\vec{x})\cdot l^3$$

Here l is the width of the grids, which is much smaller than the footprint of the light mill which is around 200 nm in our case. Field distributions are given by FDTD method, and the calculation of the Lorentz force was carried out by home-made codes. Then the torque generated by this point can be calculated from the cross product of displacement and force:

$$\tau = \iiint_V \vec{x}\times\vec{F}(\vec{x})d^3x$$

Figure 2.3 shows the simulation results of the torque at different wavelengths, with the incident light intensity normalized to 1 *V/m* for the electric field. Different colors in the simulation means different simulation conditions. For both the red and blue curve, the lightmill is embedded in dielectric material which homogenously surrounds the lightmill, but corresponds to different boundary condition. For the red curve, open boundary condition was set to the boundaries in the simulation domain, which stands for the experiment situation that only single lightmill sitting in a homogenous environment. Two peaks were found in the result, one sitting at 800 nm and the other one at 1800 nm. These two peaks match up two resonant modes, fundamental mode (1800 nm) and second mode (800 nm). Since torque is a vector, different signs stand for different directions. This means that not only the magnitude, but also the directions of the torque can be tuned by merely change the wavelength of the light.

To check the result of our home-made codes, we also calculate the optical torque on the lightmill with periodic boundary conditions, which corresponds to an infinite two-dimensional lattice of the lightmill. In this case, when the period of the lattice is smaller than the wavelength, there should be no optical torque due to reciprocity principle of optics[49]. Another way to understand this claim is that since the 2D lightmill is not chiral media as it has one mirror symmetry, the polarization of the transmitted light should not be changed. Therefore there is no angular momentum exchange between the light and the 2D lattice and the torque should be zero. Our simulation result confirms this point, as the blue curve is very close to zero, remaining only a small torque which may due to the mirror-symmetry broken by loss.

For periodic conditions, in order to generate the optical torque, one may break the symmetry more by putting the lightmill lattice in an inhomogeneous environment, for instance on the surface of dielectric material. This corresponds to the green curve in Figure 2.3, where SiO2 (n=1.5) was used as the substrate. The torque peaks were blue shifted compared to the red one, because in this case the averaged optical index is smaller as half space is vacuum.

In the simulation, the peak in the infrared region is always larger than that in the visible region. This is because that for the same intensity of the incident light, longer wavelength means smaller energy per photon and thus more photon numbers. Since each photon maximally carries $\hbar$ as the spin angular momentum, longer wavelength has the potential to provide more torque than the shorter wavelength.

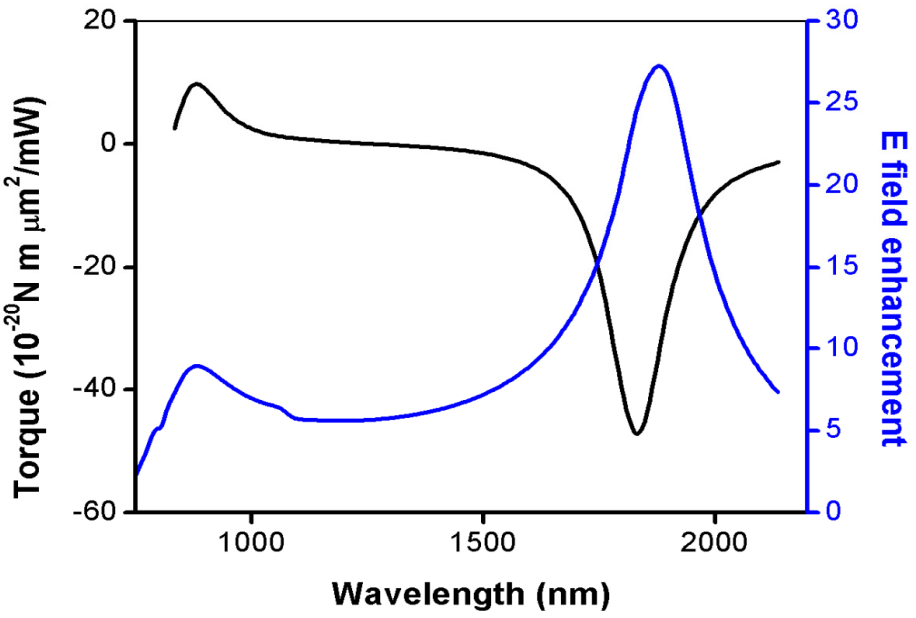

Figure 2.4 Comparison between the simulated optical torque and the plasmonic enhancement. Blue curve is the plasmonic enhancement at the gap position of the lightmill, and maximum enhancement factor of 25 can be achieved. The peak positions in the torque overlap with the peaks in field enhancement, indicating that optical torque enhancement and the plasmonic resonance are related.

For further understanding the origin of the optical torque, we also compare the torque curve with plasmonic resonance, as shown in Figure 2.4. Blue curve gives the electric field enhancement normalized to the incident light, as measured by a probe placed in the gap position of the lightmill. Two resonance peaks are found, corresponding to the fundamental mode and second mode for the plasmonic resonance. The field enhancement at Near-IR can reach as high as 25, while it is only ~ 10 for 800 nm excitation. This could because of the lower ohmic loss for metal since metal's permittivity is more negative at near-IR and more electric field is therefore outside of the metal. One may notice that there is a tiny mismatch between the peaks for optical torque and field enhancement. This is an interesting point and we are still working on.

Generally speaking, the peaks of the optical torque overlap with the peaks in electric field enhancement, which indicating that the strong optical torque of the lightmill is related with the plasmonic enhancement effect.

2.3 Orbital and Spin Angular Momentum

Free electrons in metals can be driven by the electric field of the incident light, which in turn, modifies the light by influencing the electric and magnetic field. For example, at the resonant frequency, both fields in the vicinity of the structure can be significantly enhanced, while the scattering cross section of the metallic structure is dramatically increased. The plasmonic nano-structure studied in this dissertation has two resonant wavelengths at λ_1 = 810 nm and λ_2 = 1700 nm. The corresponding currents, which indicate the motion of electrons on the metallic structure, are shown in Figure 2.5. Although the polarization of the incident light is assumed to be along x direction, the induced currents along y direction are as significant as along x. Figure 2.5c shows the Poynting vectors of the light field in the proximity of the structure. For the mode at 810 nm, the Poynting vector is found to have two components; a centripetal part at the center of the gammadion and a tangential part at the outer sides of the gammadion arms. While for the other mode, the Poynting vector mostly concentrated in the gap between the metallic arms as shown in Figure 2.5e. Since the Poynting vector is proportional to the linear momentum of light, its discontinuities at the motor surfaces induce optical pressures to the latter, providing torques counterclockwise for the mode at 810 nm and clockwise for the 1700 nm mode, although the net force keeps zero.

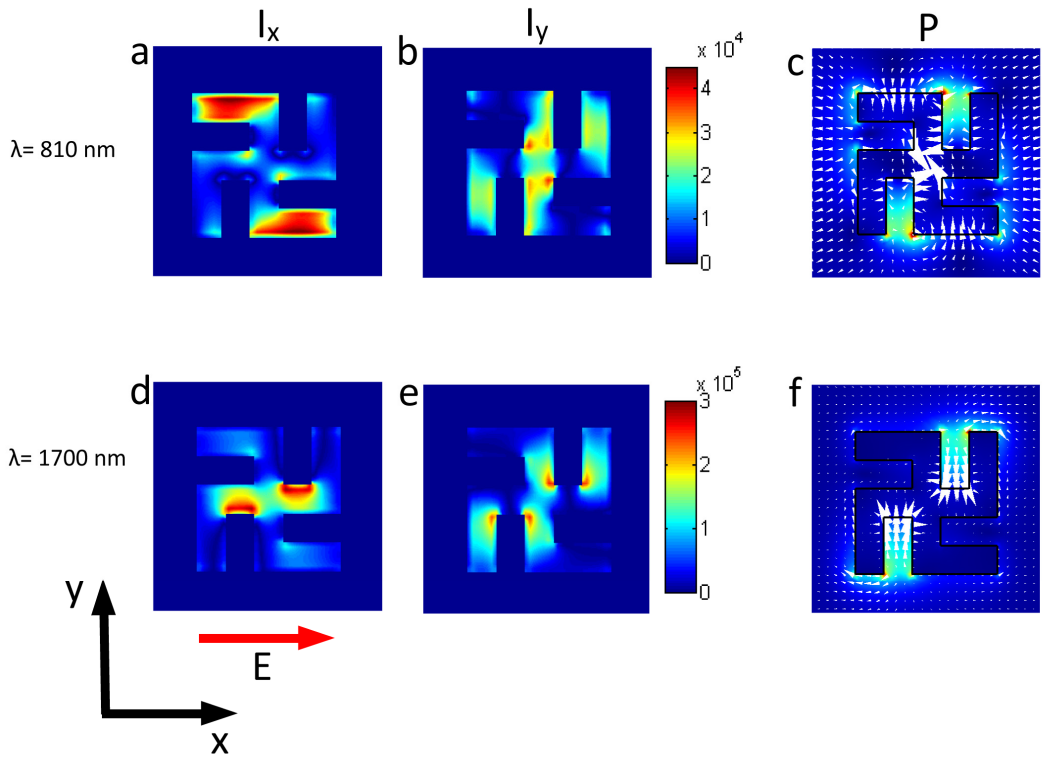

Figure 2.5 Current and Poynting vectors on a plasmonic structure at λ=810 nm and 1700 nm. a, b Amplitude of the induced current along x and y direction, respectively. **c**, The Poynting vectors and electric field. **d**, **e**, and **f** are the corresponding distributions for λ=1700 nm. **c** and **f** intuitively explain the origin of the optical torque. In **c**, the Color map shows the electric field distribution, and the white arrows indicate the Poynting flux, which is proportional to the linear momentum of light, in the vicinity of the motor. Poynting flux is scattered/absorbed at the outer side of the arms, inducing a torque on the motor to drive it counterclockwise. **f**, The same as a for illumination at λ=1700 nm; the Poynting flux passes through the gaps and scattered/absorbed by the elbow of motor, providing a clockwise torque on the latter.

As a consequence of angular momentum conservation in this process, the angular momentum of light after the interaction is also changed. Light can carry two types of

angular momentums, spin angular momentum (SAM) and orbital angular momentum (OAM). The SAM is related to the polarization state of the photon and has two eigenvalues, corresponding to left circular polarized light and right circular polarized light. For analyzing the OAM, the light field is usually decomposed into Laguerre-Gaussian (LG) modes, where the electric and magnetic vector fields in a plane perpendicular to the propagating direction can be characterized by an $\exp(im\varphi)$ phase dependence, where m is an integer number and φ the azimuthal angle. To analyze the SAM carried by the re-emitted light, we show in Figure 2.6 the far field radiation patterns for both left and right circular polarized light, at the resonant frequency $\lambda = 1700$ nm. The incident light is linearly polarized along y direction, and propagates along z. The radiation pattern has a donut shape, with the symmetric axis along y. This shape arises from the fact that the majority of the radiation comes from the dipole-like resonance along y axis of the plasmonic structure, driven directly by the incident light. We found that the radiation patterns of left and right circular polarized light are identical, indicating that the light does not carry any SAM at the far field. Therefore, the total angular momentum of the light comes purely from OAM.

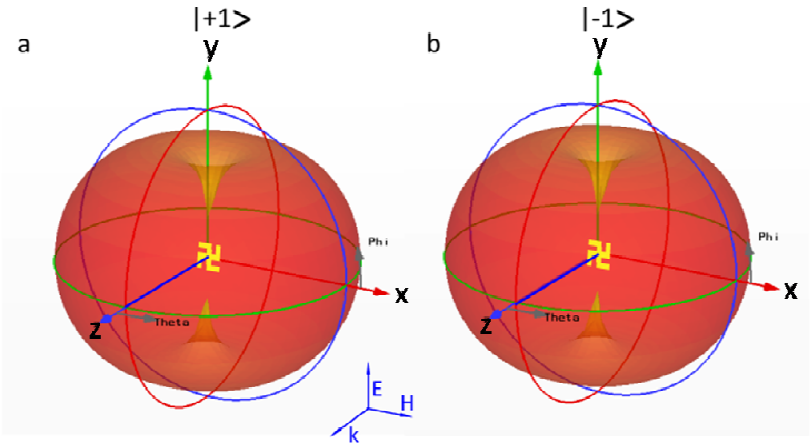

Figure 2.6 Far field radiation pattern from a plasmonic structure at resonant wavelength λ = 1700 nm. The polarization of the incident light is linear along y axis, and the propagation direction is along z. **a**, and **b** show the amplitude of the light for right and left circular polarizations in the far field, with the incident plane wave neglected. The identity of the two radiation patterns indicates that the re-emitted light remains linearly polarized.

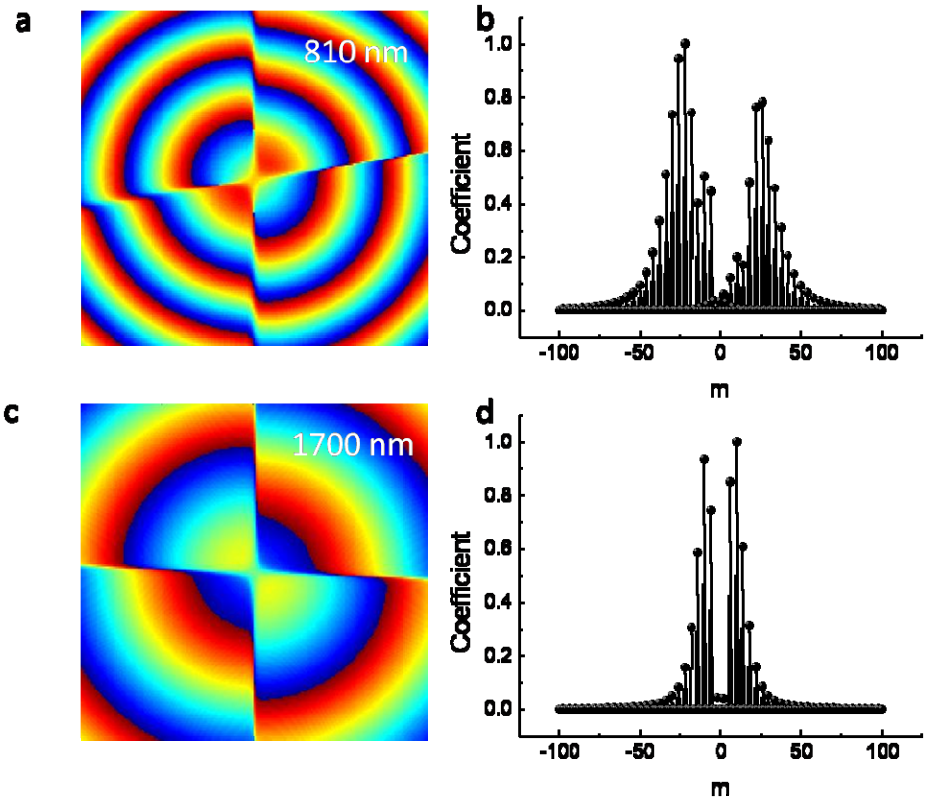

Figure 2.7 Mode analysis of the re-emitted light. a and **c** show the phase front of E_y on a plane which is perpendicular to the incident beam for λ=810 nm and 1700 nm, respectively. **b** and **d** show the decomposition of the beam profile into different azimuthal orders, showing that the photons carry unequal amount of OAM for left (negative) and right (positive) directions. The net OAM is negative for λ=810 nm, and positive for λ=1710 nm. Similar trends are also found for the E_x and E_z component of the field.

To analyze the mode distribution to the OAM, we assume a thin spherical shell around the structure and calculate the OAM carried by the re-emitted light with all polarizations. Without losing generality, we show in Figure 2.7 the phase front of the electric field in y direction at a plane perpendicular to the incident light and 700 nm behind the structure for a wavelength of λ= 810 nm and 1700 nm, respectively. The field can be decomposed

by a complete set of classic optical vortices

$$u = A_m(r,\phi)e^{im\theta}$$

Here m is a positive or negative integer and $A_m(r,\phi)$ is real. We found that the distribution is asymmetric with respect to m=0 (Figure 2.7b,d). This means that the total OAM carried by the field is not zero. For λ= 810 nm, more light is found with left-rotate OAM, while for λ= 1700 nm more light distributes in the right-rotate OAM. Similar trends can be found with E_x and E_z. Hence, the different distributions of OAM in the re-emitted light for different modes explain the different signs of the torques on the plasmonic structure, since the angular momentum of the total system, consisting of the motor and the light, has to be conserved.

2.4 Multi-motor System

Although the plasmonic enhancement effect dramatically increases the optical torque on each lightmill, a real device may still need to integrate several lightmill to achieve larger torque or broader operation wavelength range. In this section we calculate the total torque in a multi-motor system, where more than one motor is incorporated in the silica disk (Figure 2.8). We show in Figure 2.5 c and f that the optical forces on a motor are symmetric with respect to the center of the motor, i.e., they can be described as a pair of forces F_i and $-F_i$ acting on the motor *i*. Hence, the torque with respect to a certain point P outside of the motor area can be expressed by $r_{i1}\times F_i + r_{i2}\times(-F_i)$ (Figure 2.8 b).

The total torque on the system can thus be written as

$$\begin{aligned} M &= \sum_i r_{i1}\times F_i + r_{i2}\times(-F_i) \\ &= \sum_i (r_i + r_1)\times F_i + (r_i + r_2)\times(-F_i) \\ &= \sum_i r_1\times F_i + r_2\times(-F_i) = \sum_i m_i \end{aligned}$$

whereas m_i is the torque generated on a single motor *i*. This said, the total torque on the system should be the sum of the individual torques from each motor.

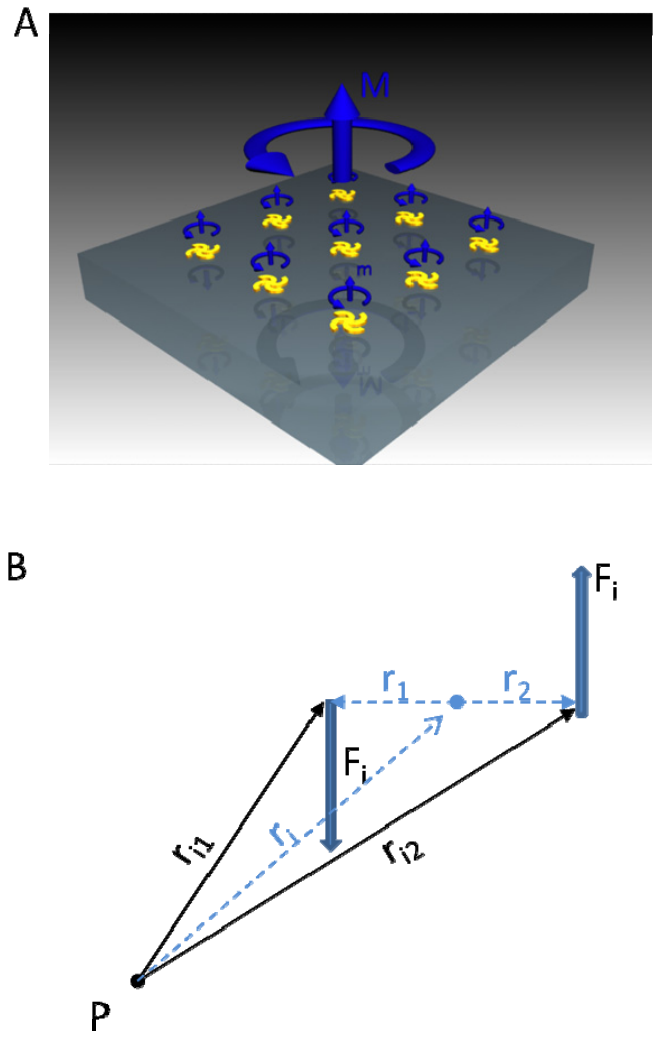

Figure 2.8 Schematic of a multi-motor disk. a, The forces on the motor can be regarded as a symmetric pair with respect to the center of the motor. Hence, the moment is independent of the reference point and the total torque on the system is the sum of the torques provided by each of the motors. **b** shows the force pair on motor *i*, with an arbitrary reference point *P*.

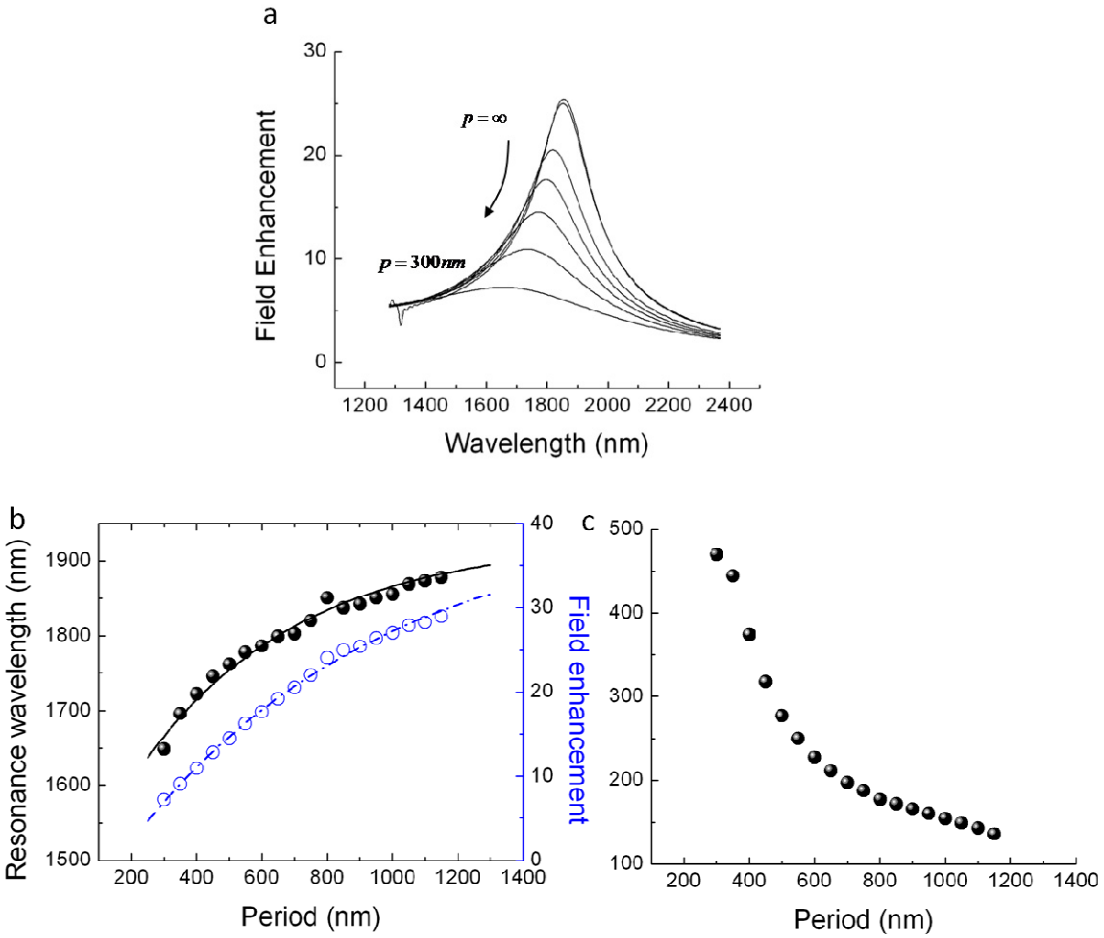

Figure 2.9 Field enhancement and resonance wavelengths for different periodicities of the multi-motor system. a, The field enhancement dependence on the wavelength, indicating the resonance frequencies. Note that the resonance is blue-shifted for smaller periods *p*. **b**, Fit of the resonant wavelength *λ* in dependents on the period *p* by the expresssion $\lambda = -485.7e^{-\frac{p}{487.6}} + 1928.4$, which is similar for other plasmonic structures.[2] **c**, FWHM of the plasmonic resonance peaks with different periods.

However, in a closely-packed motor array, the plasmonic interactions between neighboring elements should be considered. The evanescent and radiative coupling between neighboring elements leads to a modified spectral response of the periodic

pattern, resulting in weaker optical force and a shift in the resonance frequency. The spectral response dependence on the periodicity is shown in Figure 2.9. Evidently, the interactions between the plasmonic elements increase the energy of the system and shift the resonance to shorter wavelengths. Meanwhile, the electric field enhancement in the gap of the motor, which can be used as a parameter to indicate the efficiency of the plasmonic structure, is reduced from ~30 to 7. This can be understood by the fact that the scattering cross section of the motor is reduced due to the proximity to its neighboring motors. Therefore, the resonance strength of the plasmonic modes is reduced. The torque on each motor is subsequently reduced such that the 25-in-1 motor sample is only four times more efficient than the single motor, instead of 25 times as one would expect from the increased number of motors.

2.5 Polarization Influence

As mentioned in the chapter 1, we choose gammadion structure for the lightmill because of the c4 symmetry of this structure. This rotational symmetry guarantees that the mode shapes for both polarizations are identical. This is very important to keep the lightmill rotating but not trapped at a certain angle. From Figure 2.6 we already see that the far field radiation patters are the same for different circularly polarized light. Figure 2.10 shows the electric field distribution in the proximity of the lightmill, for different circular polarized excitations. From the figure we can see that the near field distributions are identical, which is because that both circular polarized light can be decomposed into two linearly polarized light. And the rotational symmetry possessed by the lightmill allows it to have the same responses to the two linear polarizations. Therefore its responses to two circular polarized light are also the same. This analysis can also be applied to any linear polarizations, or in the other words, the optical torque is a constant when the lightmill rotates.

This constant optical torque is also demonstrated in the simulation by changing the polarization direction of the incident wave. And the torque curves are almost indistinguishable with Figure 2.4. Therefore I am not plotting them here.

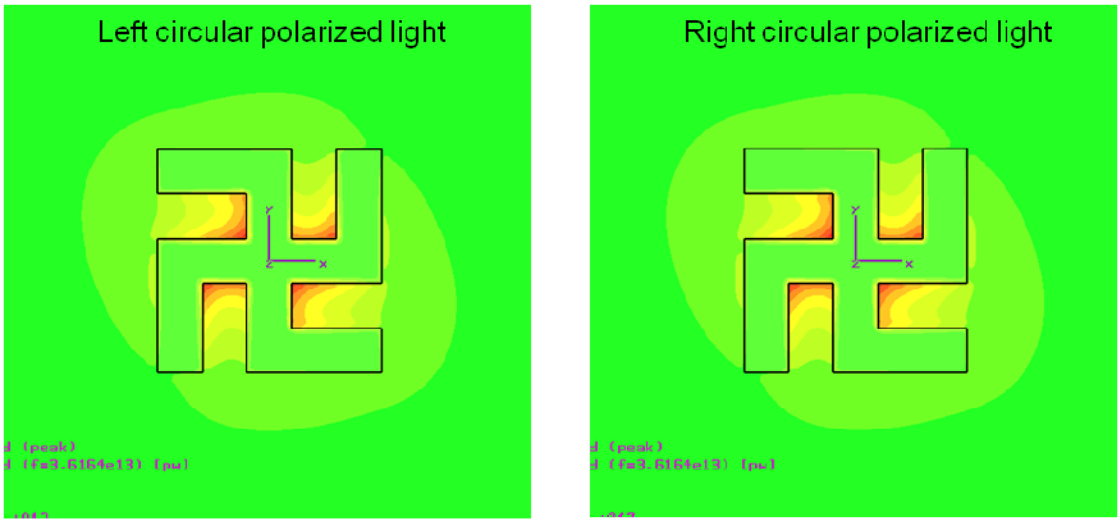

Figure 2.10 Modes excited by light with different polarizations. We can see that the near field patterns excited by different circular polarizations are almost identical. And there is only 0.1% difference if we check the raw data. This indicates that the structure is not sensitive to the polarization of the incident light, as long as the plasmonic resonance has been excited. The rotational symmetry of the lightmill allows it to be driven by both linear polarizations, as E field along x and y. Since any linear polarized light can be decomposed to these two components, the lightmill can always feel the same magnitude of optical torque, despite of its relative angle to the polarization of the light.

2.6 Transient State Analysis

As we have proven that the rotation of the lightmill is not sensitive to the polarization of the light, one may naturally come with a question: can it be rotated by unpolarized light? The answer is yes.

Figure 2.11 shows the transient state analysis of the lightmill. The field enhancement in the time domain can be calculated by the convolution between the lightmill's response and the incident light. Using a very long pulse to mimic a plane wave, we found that a lightmill needs only a few cycles to establish the plasmonic resonance. Therefore a short pulse, such as a fs laser, can also generate the torque.

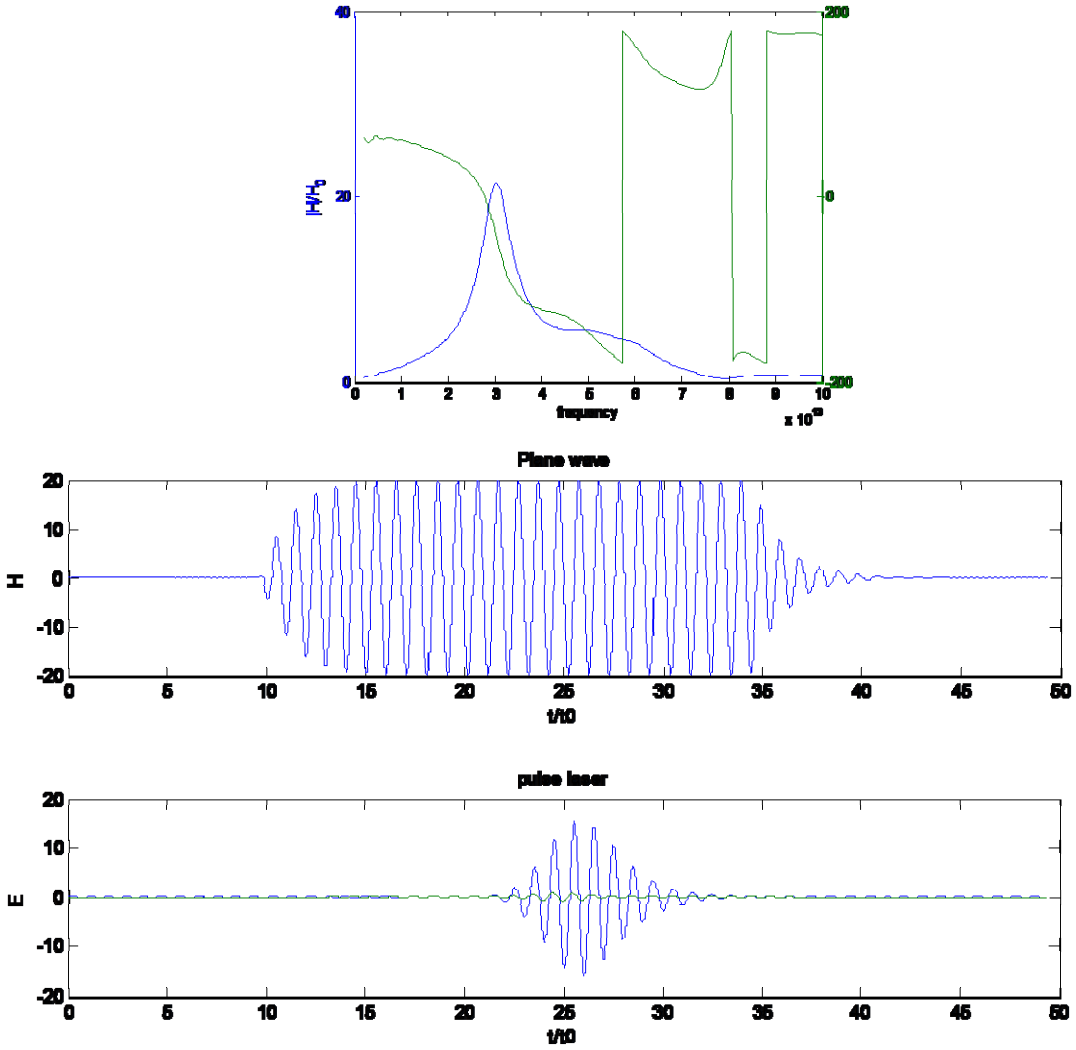

Figure 2.11 Transient state analysis of the lightmill. Top, the magnetic field enhancement factor and its arbitrary phase. Middle, the lightmill response to the "plane" wave. Here we use a relatively long pulse to mimic the plane wave. And we may see that it took only a few period for the lightmill to setup plasmonic resonance. In the bottom figure, we can see that even a very short pulse with only a few periods can excite the strong resonance as well.

In summary, we discuss the possibility to generate optical torque on a lightmill. We found that not only the magnitude, but also the directions of the torque can be controlled by changing the frequency of the incident light. We found that the torque is not sensitive to the polarization, has no requirement to the coherent length, which makes it possible for solar energy harvesting and many other tasks.

Chapter 3

Plasmonic Motor: Experiment and Results

In this chapter, we will discuss the experiment approaches we used to measure the optical torque on single/multiple lightmills. And then we will discuss the side effects in the measurement, such as plasmonic heating effect and Brownian random motions.

3.1 Experiment Approaches

As we have simulated in last chapter, the optical torque on the lightmill is dramatically increased due to plasmonic enhancement. However it is still relatively weak and needs careful experimental designs for measuring. In this section we will discuss the different approaches we have tried.

In the first trial, we put the lightmills on substrate, and shined the laser directly to drive it. The lightmill size is 2 μm, and the working wavelength was designed for CO2 laser at 10.6 μm. Four small tips are fabricated on each arms of the lightmill by over dosing the PMMA[50]. And then a transferring technique[51] is applied to turn over the samples, letting the tips to contact with the substrates in order to reduce frictions. Figure 3.1 shows the samples after they have been turned over. Unfortunately, from literature we found that only in very critical situations people can reduce the friction to nearly zero[52,53], and the frictions in our case is too large for the optical force to conquer.

In the second trial, we moved the lightmill from the solid substrate to a liquid surface (water), where the lightmill can move freely. And by modifying one surface of the lightmill with hydrophobic molecules[54], we can form a Langmuir-Blodgett (LB) monolayer of lightmills at the interface between air and water. However later we found that the Marangoni forces[55], gradient of surface tension due to temperature differences, will also generate torque and cannot be excluded in the final result. Another limitation comes from the strong absorption of water to the IR light, which makes it difficult to trap the lightmill by light.

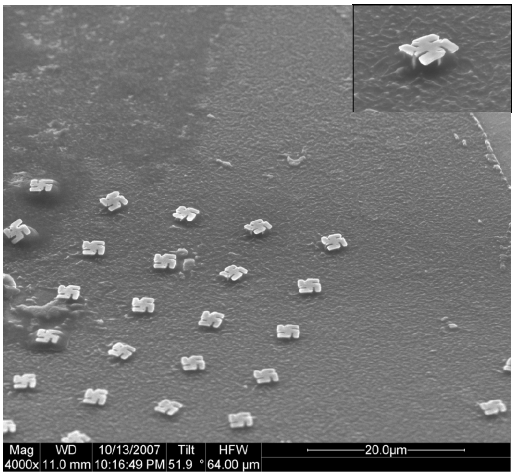

Figure 3.1 1st trial. To rotate the lightmill on the substrate. The size of the lightmill in this case is around 2 µm, and the resonance wavelength is designed for 10.6 µm. Inset shows the zoom in of a single lightmill, which is lifted up by four tips to reduce the friction. Different substrates have been tried, but the friction cannot be reduced to less that pN, which is about the up limit we can provide by single lightmill.

In the third trial, we sank the lightmills (2 µm) to the bottom of the solution, which has been changed from water to CS2 in order to reduce the absorption of IR light. However this time the problem comes from the substrate, where absorption remains large with any kind of substrates, including CaF2, MgF2, CdS and others. Heating of the substrate will generate local liquid flows which blows the lightmill away.

In the first 3 unsuccessful trials we always used lightmill with the size of 2 µm not only because it is easier to fabricate, but also because of two advantages in the following measurement. Firstly, a particle with the size of 2 µm is larger than the diffraction limit and can be clearly observed by a normal optical microscopy. Secondly, the Brownian motion, which is only related to the size of the particle, can be considerably reduced when the size of the particle is larger than 1 µm. Both of these advantages made us reluctant to reduce the size of the lightmill at the beginning.

In the fourth experiment, we successfully reduced the size of the lightmill without losing the previous two advantages. We integrated the nano-scale lightmill into a dielectric disk, which can reduce the Brownian random motion, and also can be used as an indicator for

the rotations. In next section we will talk about the fabrication process.

3.2 Fabrication Procedure

Figure 3.2 shows the 5 major steps to fabricate the nanoscale lightmill. Table 3.1 lists the details of the fabrication process.

STEP	M/C	RECIPE	REMARKS
Prepare Substrate	PECVD	200 nm Si	SiO2 on the top of Si.
		200 nm SiO2	
Fab lightmill	E-beam litho	Crestec, PMMA A3 4000 rpm	Quality of Au is critical.
	E-beam depo	30 nm Au	
Fab SiO2 disk	E-beam litho	2.2 μm square disks	Cr on the top of SiO2 for masking
	E-beam depo	300 nm SiO2, and 50 nm Cr	
Etch SiO2	Plasma etch	Etch 300 nm SiO2	Remove Cr after etch
Release sample	XeF2 etch	3 min to remove Si layer	

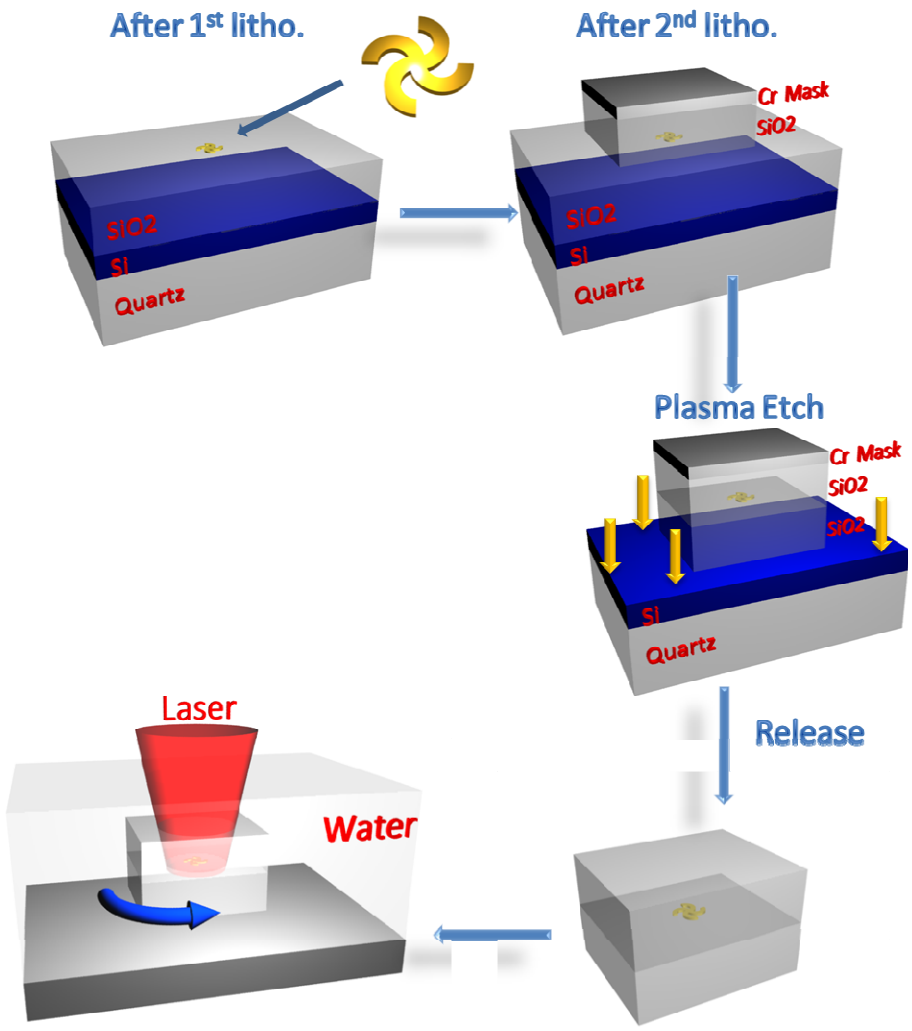

Figure 3.2 Schematic of fabrication process. a, Glass slides, pre-deposited by 200 nm poly-Si and 300 nm SiO_2, are used as substrates. Single/multi gold motors are patterned by e-beam lithography on the top of the substrates. **b,** Silica disk is patterned at the same position by EBL using alignment marks together with a Cr mask for etching. **c,** CHF_3 plasma etching transfers the pattern to the pre-deposited silica slab to generate a homogeneous environment for the gold gammadions. **d,** Cr etchant and XeF_2 dry etching are employed to remove the Cr mask and Si sacrificial layer. The adhesion keeps the silica disks on the cover glass. **e,** Finally, the measurement is carried out in DI water.

All samples are fabricated using standard electron beam lithography (EBL) and consist of plasmonic nano-structures symmetrically sandwiched between two SiO_2 layers. The full fabrication procedure is illustrated in Figure 3.2. Pre-cleaned glass cover slip substrates are coated by 200 nm poly-silicon and 300 nm SiO_2 using plasma-enhanced chemical vapor deposition (PECVD) and electron-beam thermal evaporation, respectively. The poly-silicon is used as a sacrificial layer to release the microdisk samples at the last step from the glass substrate. The substrate is then coated with 3% polymethyl methacrylate (PMMA), followed by a 7 nm chromium layer to provide a conductive surface for the EBL (Crestec CABL-9510CC High Resolution Electron Beam Nanolithography System). After the gammadion-shaped plasmonic nanostructures (size ~ 190×190 nm²) are exposed and developed with MIBK, 1 nm Cr and 30 nm Au layers are deposited by electron-beam thermal evaporation followed by a lift-off process for the remaining PMMA. The sample is then coated again with 11% PMMA and the silica disks (size 2.2×2.2 μm²) are defined by a second EBL process. Another 300 nm SiO_2 layer is then deposited to provide the upper part of the microdisks. To transfer the disk shape to the SiO_2 we use an additional 50-nm-thick layer of Cr as a mask for the final etching step by a CHF_3 plasma etch (Figure 3.2c). Finally, the Cr layer is removed by Cr etchant (Cr-7), and the sacrificial poly-silicon layer is removed by dry etching with XeF_2. After the etching the microdisk samples with the plasmonic gammadions lie freely on the glass substrate.

After the fabrication, the lightmill is embedded in the middle of two SiO2 disks. These two disks give a homogenous environment to the lightmill, which is therefore not a chiral media and makes our experiment suitable for universal case.

One more thing need to address is that the quality of the gold is very critical to the performance of the lightmill. High vacuum is needed during the deposition, and post-deposition treatment[56] is recommended as well.

Figure 3.3 shows the scanning electron microscope (SEM) picture of the prepared sample. The lightmill, which has higher contrast compared with the surrounding dielectric, is embedded in the center of two SiO2 disks. It is brighter because gold has larger scattering cross section for the secondary electrons compared with SiO2. The total thickness of the SiO2 disk is changed from 200 nm to 800 nm to find the optimized thickness for trapping. We found that ~400 nm is the best thickness for this purpose. Thinner thickness will provide less trapping force to cancel the scattering force on the lightmill, which is significantly increased at the resonance frequency. On the other hand, thicker SiO2 is more likely to turn over, since it is more “isotropic” as the thickness comparable with the footprint.

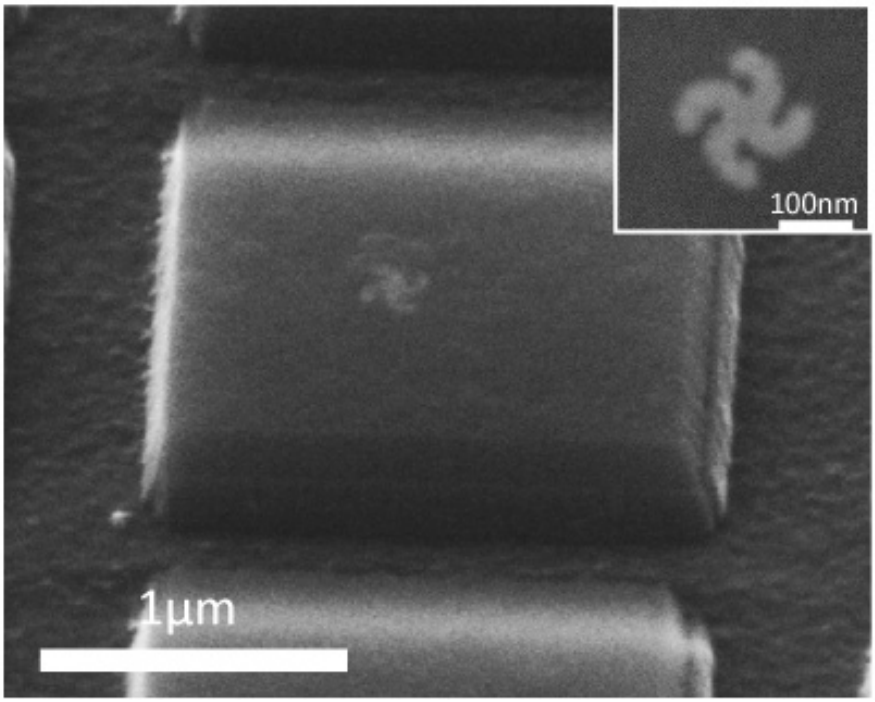

Figure 3.3 Scanning electron microscope (SEM) pictures. Inset shows the zoom-in of the nanoscale lightmill. The line width of the lightmill is 38 nm, with the thickness of 30 nm. The SiO2 disk sits on Si substrate, which is later used as a sacrificial layer to release the samples. The optimized thickness of the disk is around 400 nm, and in the SEM it is only 200 nm for better contrast and resolution of the lightmill. If the SiO2 disk is too thin, it may not provide sufficient trapping force in the focused light beam to cancel out the scattering force on the lightmill. While if it is too thick, it can easily be stuck up by the incident light.

3.3 Experiment Configuration

For the experimental investigation the silica microdisks are dispersed into de-ionized (DI) water between two glass slides. Due to the gravitational force the microdisks preferentially sink to the bottom glass slide and stay there rather than suspending in the solution. Hence, the gravitational force keeps the silica microdisks horizontal and the gammadions normal to the incident light which is illuminated from the top. The size of the silica disk also helps to reduce the Brownian motion by 3 orders of magnitude which

otherwise would be result in an uncontrolled change of the orientation of the small gammadion. The thin water layer that is formed between the silica microdisk and the quartz substrate reduces the friction between the disk and the substrate. Therefore, the viscous drag becomes the only limitation of rotation. Under the condition of a laminar flow (low Reynolds number, $\sim 10^{-5}$) the surface roughness and fine structure of the silica microdisks are not important, and the friction can be estimated by:

$$f = 32/3\pi\mu\omega a^3$$

Here μ is the viscosity of the water, a is the radius of the disk and ω is the rotation speed.

To measure the rotation speed of the dielectric disk powered by lightmill, we use an experiment setup as sketched in Figure 3.4:

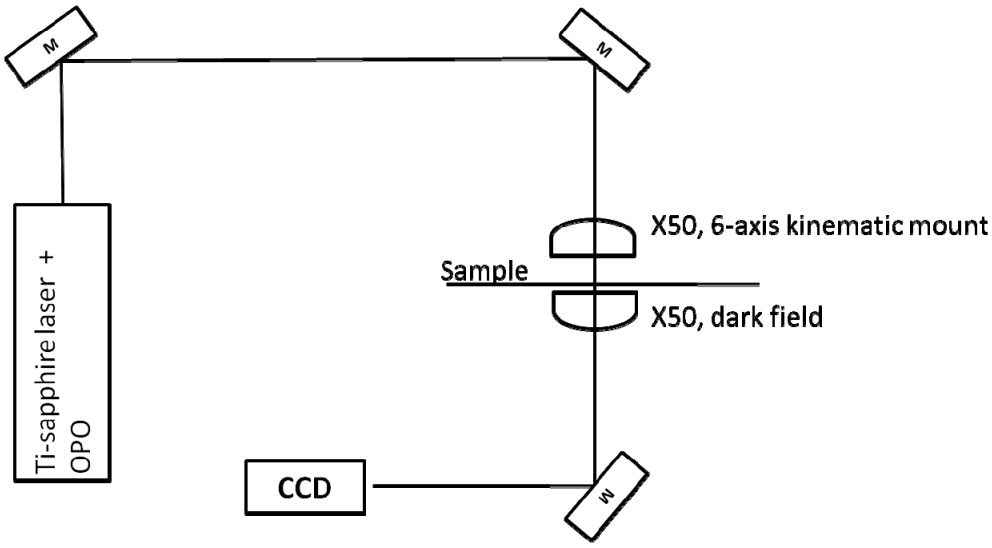

Figure 3.4 Experiment setup. A femto-second Ti-sapphire laser is used to provide tunable laser with the wavelength around 810 nm. Then an optical parametric oscillator (OPO) is used to generate the pulse laser with wavelength from 1200 to 1800 nm. Then the beams are sent into a typical optical-tweezers setup, and the same beam is used for both trapping and rotating the particles. Then another objective lens projects the image to a CCD and the movements of the particles are recorded.

A femto-second Ti-sapphire laser is used to generate the tunable laser pulse with the wavelength in the range of 750 to 850 nm. Then the major portion of the laser pulse is sent into an optical parametric oscillator (OPO) to provide photons in the range of 1200 nm to 1800 nm. The rest portion of the first beam is then collimated with the second laser beam from the OPO, and a flipper mirror is used for switching between these two. A typical optical-tweezers setup is used for the measurement. The laser beams are sent in via the top objective lens, which is carefully aligned to the laser beam with a 6-axi kinematic mount to avoid any potential torsion to the beams. Then the high NA objective length focuses the incident beam and forms the optical potential.

Instead of using an extra laser (usually at 980 nm) to trap the particle first, we use the same light beams for both trapping and rotating. Therefore the NA of the top objective lens is critical. For normal optical trapping, high NA objective lens is preferred because it may focus the light tighter and therefore the trapping force can be stronger. However, to a dielectric disk, the situation is much more complicated[57]. When illuminated by a focused light beam, a dielectric disk always prefers to stand up and make its plane parallel to the laser beam, in a manner that it can feel more laser beam and reduce larger optical potential. The only force to conquer this effect is the gravity on the dielectric disk. After trying different objective lenses, we found that NA~0.5 gives the best balance between the trapping force and the gravity for the present sample parameters (2.2 μm in length and 600 nm in thickness).

The movement of the dielectric disk is then projected by another objective lens to a charge-coupled device (CCD) for recording. Dark field microscopy is preferred in this step for better imaging quality.

3.4 Experiment Results

3.4.1 Sequencing images

Figure 3.5 presents sequencing images of the microdisk in DI water rotated by a linearly-polarized Gaussian beam. Figure 3.5a depicts a single plasmonic motor 100 nm of radius, rotating a 2.2x2.2 μm² disk when illuminated by a beam of 1 mW power at 810 nm wavelength, focused by an objective lens with NA=0.5. The lightmill is represented as a bright spot because that it is already under the diffraction limits, and no details can be observed by the optical microscopy. Its rotation can only be derived by observing the rotation of the SiO2 disks, which shows clear edges in the dark field microscopy. The disk rotates at 0.3Hz counter-clockwise. When multiple motors are integrated into one

silica microdisk, the torques applied on the disk from the individual motors accumulate and the overall torque is increased[58]. This is demonstrated in Figure 3.5b, where a silica disk with 4 motors attains the same rotation speed *with only half of the laser power applied*.

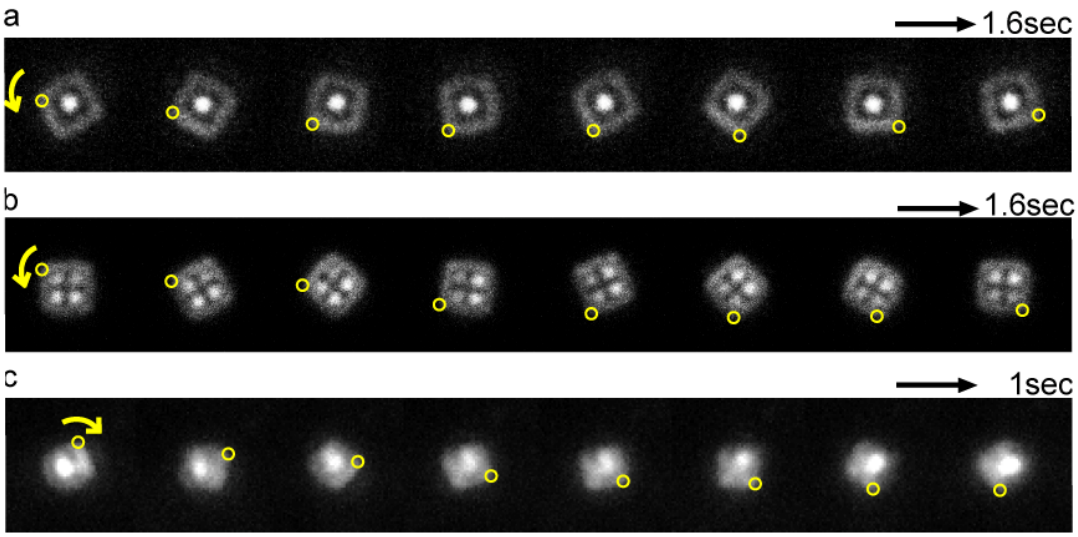

Figure 3.5 Sequencing dark-field microscopy images of a rotating silica microdisk, driven by plasmonic motors. a, A single motor illuminated by a λ_1 = 810 nm laser beam drives the disk rotating in a counterclockwise direction. **b**, A 4-in-1 motor sample rotates counterclockwise under the excitation at wavelength 810 nm. Although they rotate at similar speed, 4-in-1 sample requires only half light power of single motor sample, which indicates that higher torque can be achieved by integrating more motor into one device. **c**, A laser beam with λ_2 = 1700 nm in wavelength induces a clockwise rotation for the same disk as **a**. In Total times for three series are 1.6 sec, 1.6 sec, 1 sec in sequence, with laser powers 1 mW, 0.5 mW and 3 mW respectively (NA=0.5). The beams are generated by a femto-second Titanium-Sapphire oscillator and a synchronously pumped optical parametric oscillator, respectively. The bright spot in the center of the silica disk results from the strong scattering from the plasmonic motor, though the fine details of the structure can not be observed by optical microscope due to diffraction limit. The silica disks are trapped by the same light beam.

Interestingly, the rotation direction of the motor can be controlled merely by changing the wavelength of the light. When illuminated with a similar linearly polarized Gaussian beam but at 1700 nm wavelength, the same single-motor rotates clockwise (Figure 3.5c). Namely, the rotation is a direct result of the torque generated by different plasmonic modes resulted from the interaction between the light and the motor, and does not stem from a pre-determined angular momentum of the light, nor from plasmonic heat effect inducing water flow. It agrees well with our simulation predictions in chapter 2.

3.4.2 Rotation speed under different wavelengths

To measure the rotation speeds of the lightmill close to the resonance frequencies, single lightmill can no longer fulfill the job since its maximum rotation speed is already too low at the resonance frequency. To increase the rotation speed, one way is to increase the laser power, and the other way is to integrate more lightmills in each dielectric disk. Increasing power will potentially damage the lightmill and we already found that the threshold before damaging the lightmill is about 10 mW in our setup. And the only way to increase the speed is increasing the number. We have proven in last chapter that the optical torque generated by different lightmills will not cancel each other, but sum up.

Figure 3.6 is the SEM pictures of the prepared multiple-in-one lightmill samples, before they are released from the Si substrate. 25 lightmills, forming a 5 by 5 matrix array, are embedded in the SiO2.

The correlation between the plasmon resonances and the light-induced torque is well manifested in the relations between the measured transmission spectrum (Figure 3.7e) and the frequency-dependent angular velocity of the rotated sample (Figure 3.7d), where the resonance frequencies whose the absorption is strongest are found to be the same as those exhibiting the rotation speed maxima. Note that such closely-packed array of plasmonic elements exhibits strong coupling between the modes of the individual motors when the spacing between the motors (100 nm) is much smaller than the light-motor interaction cross section [~600 nm[59]]. This results in a transition from a single resonance to an absorption “band”, mostly pronounced for the fundamental resonance around 1500 nm, where the strong coupling results in additional higher-energy. This additional evidence shows that the torque indeed originates from the plasmonic resonance.

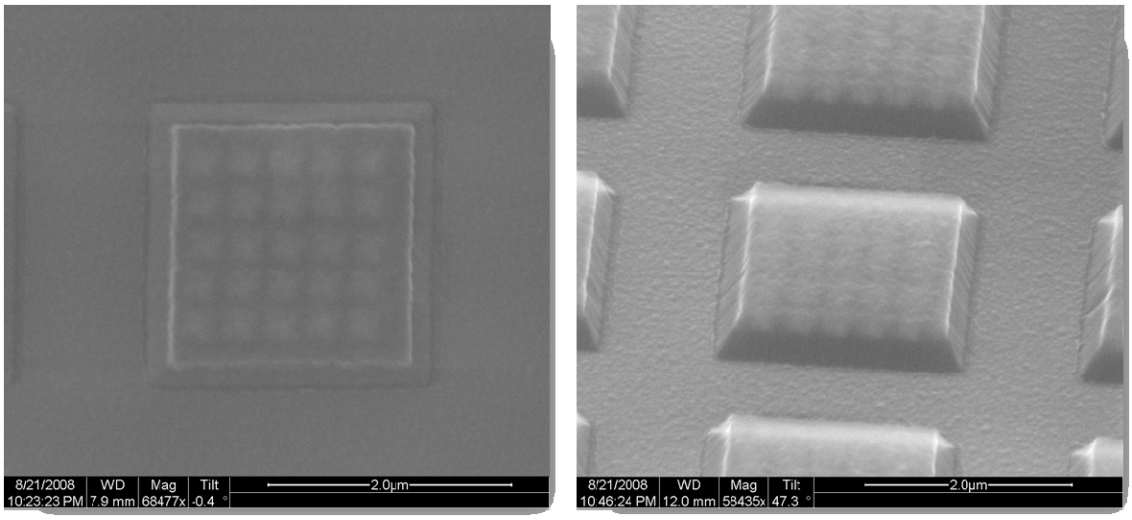

Figure 3.6 SEM pictures of 25-in-1 disks. Left, top view of the sample. Right, side view of the same sample. 25 lightmills, forming a 5 by 5 matrix array, are embedded in the SiO2. The linewidth of the lightmill (50 nm) is slightly larger than that of the single lightmill (38 nm). The distance between two adjacent lightmills is 400 nm. The size of the dielectric disk is still 2.2 µm, with the thickness around 400 nm.

The optical torque exerted on the silica disk can be found from the measured angular velocity, using the classical equation of motion

$$I\frac{d\omega}{dt}+\gamma\omega=\tau_{motor}$$

Here, I is the momentum of inertia of the silica disk, ω is the rotation velocity, γ is a damping term originating from water viscosity, and τ_{motor} is the torque provide by the light-motor interaction.

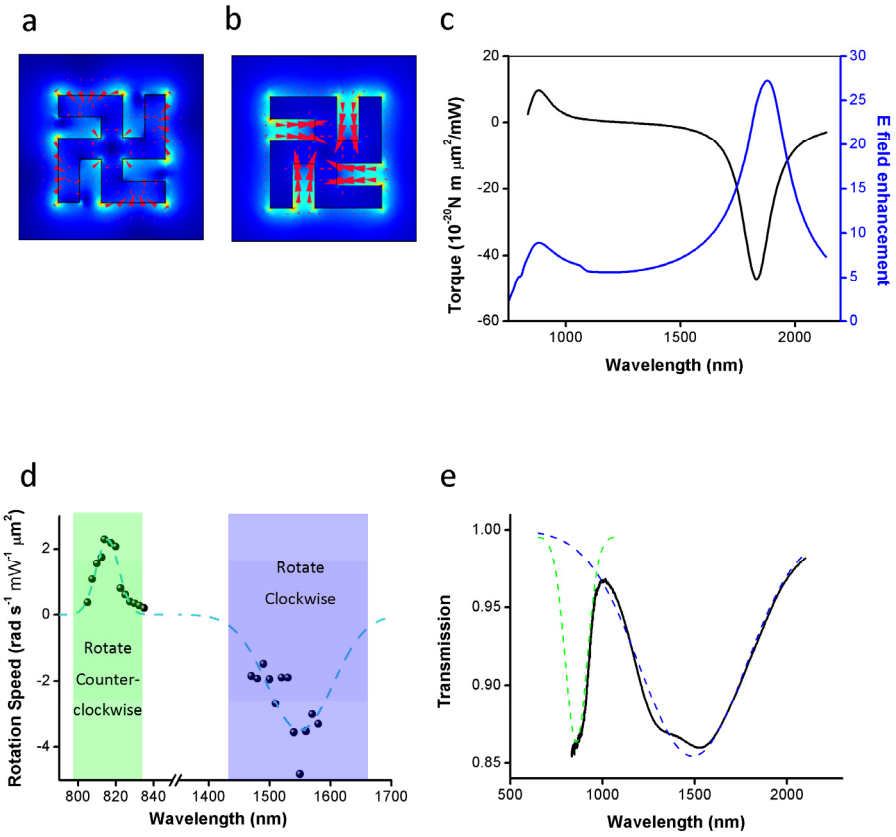

Figure 3.7 Rotation characteristic and optical properties of the motors. a, The electric field and pointing vector induced on the motor at illumination wavelength of λ=810 nm. The Color map shows the electric field distribution, and the red arrows indicate the Poynting flux, which is proportional to the linear momentum of light, in the vicinity of the motor. Poynting flux is scattered/absorbed at the outer side of the arms, inducing a torque on the motor to drive it counterclockwise. **b**, The same as a for illumination at λ=1700 nm; the Poynting flux passes through the gaps and scattered/absorbed by the elbow of motor, providing a clockwise torque on the latter. **c,** torque calculations on single light-mill show a positive and negative torques at the plasmonic resonance frequencies (visible and near IR, respectively). **d**, The measured variation of the rotation speed with the wavelength of excitation beam of a 25-in-1 light-mill sample. Positive rotation corresponds to counterclockwise rotation, and vice versa. **e**, Transmission spectrum of a 25-in-1 light-mill sample, measured by Fourier Transform Infrared spectroscopy (FTIR). The solid line corresponds to the measured spectrum while the dashed lines have been added to fit the spectrum with the 2 resonant dips corresponding to the two plasmonic modes; one in visible range (green), and one in near-IR (blue).

Due to the low Reynolds number in our system (~10^{-5}), the surface roughness and fine structures of the disk become insignificant, hence it can be approximated as a cylindrical disk with radius a where its damping coefficient becomes

$$\gamma = \frac{32}{3}\pi\mu a^3$$

μ is the water viscosity[60]. At steady state ($t \to \infty$), we obtain a single motor torque of τ_{motor} =140 pN·nm for 1 mW/μm^2 incident intensity at the resonance wavelength, providing a driving power of 1.7 eV/s.

3.4.3 Influence of Plasmonic Heating Effect

Plasmonic resonances are always accompanied by heat generation due to the ohmic losses of the metal that leads to energy dissipation. Destructive applications, like denaturation of proteins and thermal ablative therapy for cancer, have been proposed to utilize such thermal heating effect of plasmonic resonances. However, in our experimental approach, the generated heat can provide a temperature change to the surrounding water and potentially lead to a convection of the water itself as shown in Figure 3.8a. Such a water flow can lead to a torque if the friction on the side walls is not symmetric with respect to the center of the particle.

We use a finite element analysis tool (COMSOL) to demonstrate that there is no torque induced by the convection in the heated water in our system. We calculate the temperature distribution in the silica microdisk containing a single motor for a resonant excitation of the plasmonic mode. A plane wave with power intensity of 1.6 mW/um^2 and wavelength of 1715 nm is used to excite the plasmonic resonance in the motor, where the ohmic loss in the metal is used as the thermal source in the heat transfer simulation. Figure 3.8b shows the obtained temperature distribution on the surface of the silica disk. We find that the temperature is symmetrically distributed on the silica disk surface and cannot generate non-symmetric water convections around the disk.

This analysis shows that thermal effects, like convection of the heated water, do not play a role in the optically-induced torque in our system and that the torque arises solely from the strong light-matter interaction with the plasmonic nanostructure.

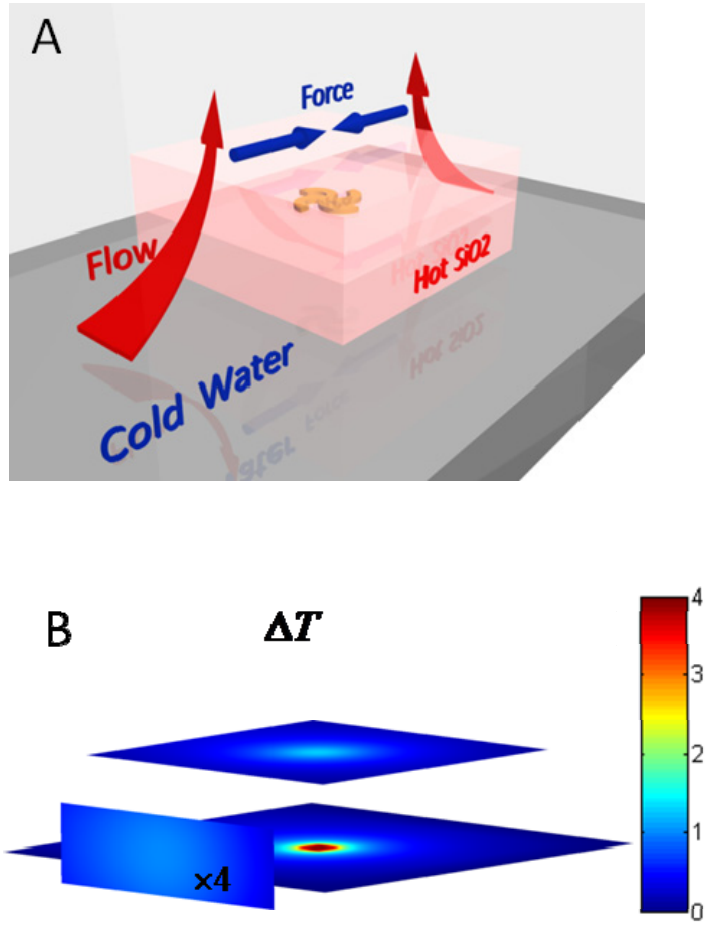

Figure 3.8 a, Illustration of the friction force generated by heat-induced water flow. Owing to the ohmic loss of the plasmonic structure embeded inside of it, the silica disk has higher temperature than the water and induces convections. In **b** we show the temperature change on the motor and on the side walls of the silica disk. By assuming the incident light to be the same density as in the experiment (1715 nm, 1 mW, NA=0.5), we find that the temperature change on the motor is about 4 degrees. The temperature distribution on the surface of the disk is symmetric to the geometry center, which indicates that the water flow is also symmetric and the time averaged torque from the flow is zero.

3.4.4 Brownian Random Motion effect

Brownian motion for a micron particle in the solution is inevitable, so is the Brownian rotation. This random rotation may introduce significant errors in the measurement, especially when the disk is rotating slowly. By increasing the size of the disk from 200 nm (lightmill) to 2.2 μm (microdisk), the random rotation is reduced by orders.

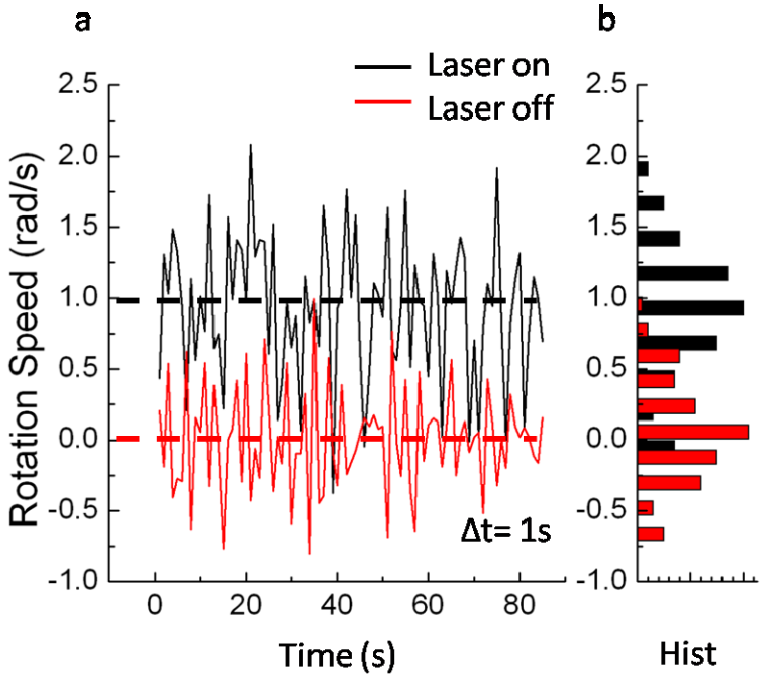

Figure 3.9 Brownian motion effect on the dielectric disk. By increasing the size of the sample from 200 nm (lightmill) to 2.2 μm (microdisk), we have already successfully decreased the magnitude of the Brownian motions. And the rotation speed with and without laser can be clearly separated from each other.

Figure 3.9 shows the real time rotation speed with and without laser (810 nm). It is calculated from the video of the movement, with the time step set to 1 second. The random speeds in the red curve are induced by the Brownian rotation, but the averaged effect of this random rotation is zero, which means that in a long term the sample did not

show any trend to rotate along any direction. When the laser is on, we can see that the averaged speed is non-zero. Although occasionally the speed is negative, which means it rotated backward under the influence of the Brownian rotation, the averaged effect is rotating forward.

To conclude, in this chapter we experimentally showed that a nano-scale plasmonic element can provide an optical torque sufficient to rotate micrometer-sized dielectric samples when illuminated with a plane wave or Gaussian beam. The unique plasmonic mechanism is manifested in the enhanced cross-section of the light-matter interaction and the ability to fully control the rotation speed and direction by merely tuning the illumination wavelength. This demonstration opens exciting possibilities in nano-electro-mechanical systems, energy conservation and biological applications, where the small motor size can make it useful for in-vivo manipulation such as controlled winding and unwinding DNA by illuminating at different frequencies.

Chapter 4

Optical Force Between Plasmonic Particles

Optical force in the nanoscale is of fundamental importance. Although the binding forces between waveguides, or cavities have been intensively studied in recent years, the direct measurement of the optical force between two plasmonic particles have not been demonstrated, due to experiment difficulties. In this chapter, we will discuss the simulation of the interaction between plasmonic particles, and preliminary results for measuring this force.

4.1 Background Introduction

4.1.1 Optical Force in Optomechanical Systems

The optical force is of fundamentally important for light-matter interaction, and has been widely studied after the invention of optical tweezers. However, to harness this optical force, which will allow solid state devices to work under new physics principles, is still facing a significant challenge. This is because that the two major mechanisms for optical forces – radiation pressure and transverse gradient force – are both relatively weak and hard to be utilized.

One way to increase the light-matter interaction is to use high Q cavities[61], which confine photons to small volumes and increase the force for per photon. Such forces have recently been proposed and demonstrated for constructing novel optomechanical components, for instance tunable lasers, couplers and filters[12,62,63]. In the latest research, the interaction between a low Q cantilever and the substrate, through the gradient of the evanescent wave, has also been demonstrated[64]. However, to reduce the system into nanoscale remains challenging, since the weak interaction asks for elegant measurement technique, sophisticated optical design, and stringent fabrication. And therefore it remains an open question.

As we have demonstrated in the previous two chapters, plasmonic resonance can spectacularly enlarge the scattering cross section[59] and the plasmonic force are enhanced

due to field enhancement and gradient of evanescent wave. These features make the plasmonic particles perfect candidates for studying the optical interaction within the optomechanical system, and also possess the potential to drive the future Microelectromechanical systems (MEMS) devices.

We choose split-ring resonator pairs as our candidate to study the optical interactions. Compared with other plasmonic structures such as bowties[65] or Pi structure[66], split ring pairs have the advantages as longer working distance, and stronger binding forces. For bowtie structures, the field with the gap is strongly enhanced only when the two parts are relatively close to each other, and the intensity drops dramatically when the distance is larger than 20 nm. The advantage for a Pi structure is that the interaction could be both positive and negative, which means both attracting and repelling forces can be achieved. However this structure is also very sensitive to the distance between the bright bar and the dark bars, and requires strict tolerance for fabrications.

We use a different code as previous simulations to evaluate the optical force between two split ring particles. Instead of calculating the Lorentz force on each points of the split rings, we used Maxwell's stress tensor which is more compact for calculating force. Figure 4.1 shows the simulation result of the plasmonic force. The split rings are placed in the same plane, whose normal direction is also the propagating direction of the incident light. The size of the lightmill is 150 in length, 50 nm in line width, and 30 nm in thickness. The intrinsic plasmonic resonance wavelength of this split ring in the vacuum is around 1250 nm, which is used for the incident light as well. The linearly polarized incident light has the electric field assigned along y direction, to excite the plasmonic resonance more efficiently.

The split rings are shifted 200 nm along y direction to each other, and their distance along x direction is changed from - 1 μm to 1 μm. The optical force, calculated by integral of the Maxwell's tensor along a box's surfaces which surround the split ring, is plotted in Figure 4.1. Different colors in the figure represent for different force components. The red curve (Fz) is always non-zero because that the scattering force on the plasmonics always exists. Green curve (Fy) is negative means that the force along y direction is attractive. Blue curve (Fx) changes signs after the split rings pass each other.

In the simulation, the intensity of the incident light is normalized to 1 V/m, which equals to $3mW/m^2$. Since a tightly focused laser beam can easily reach $10^{13} mW/m^2$, the maximum force between the two plasmonic resonators are expected to be the level of a few pN, with the working distance as large as 100 nm.

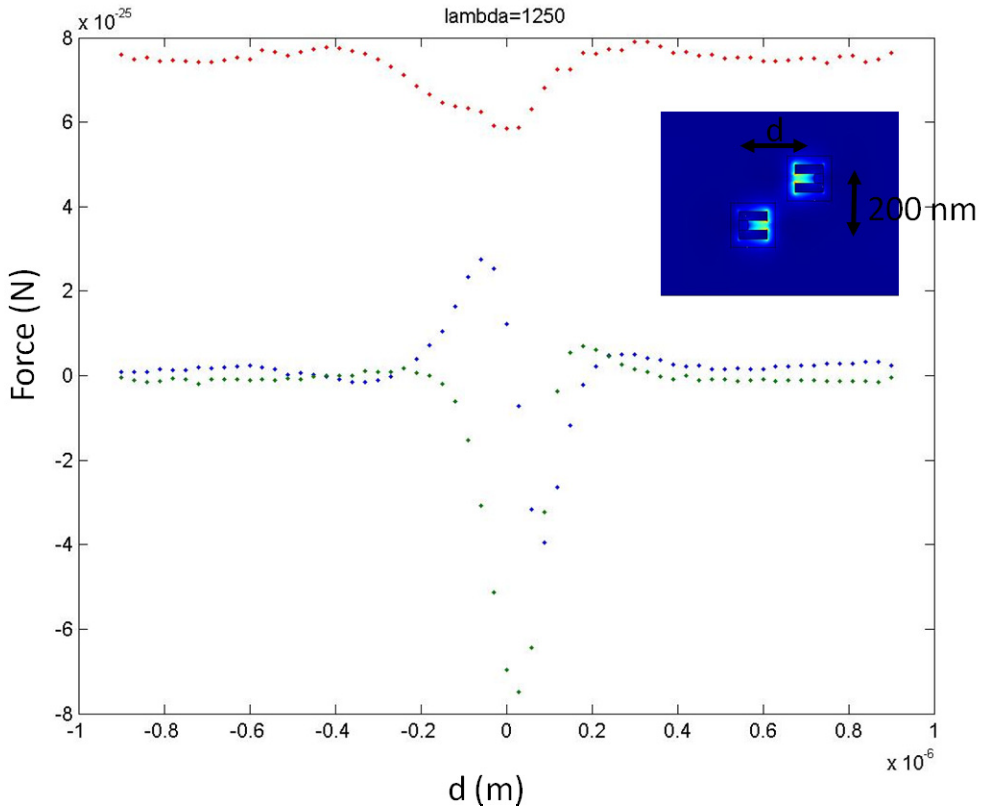

Figure 4.1 Optical force between two plasmonic split rings. The size of the gold split ring is 150 nm, with the thickness of 30 nm. The electric field of the incident light (1250 nm for the resonance case) is normalized to 1 *V/m*. One split ring is shifted along y direction from the other for about 200 nm, and their distance along x direction is varied from negative 1 μm to positive 1 μm. The optical force on the bottom split ring is plotted in the figure, with different colors indicating different force component. Blue, green, and red curves stand for forces along x, y, and z directions, respectively. Simulation is carried out by COMSOL, and the force is calculated by integral Maxwell's stress tensor along box surfaces, which surround one of the split rings. The red curve (Fz) is always non-zero because that the scattering force on the plasmonics always exists. Green curve (Fy) is negative means that the force along y direction is attractive. Blue curve (Fx) changes signs after the split rings pass each other.

4.1.2 Experiment Approach

As we have simulated, the amplitude of the optical force is only a few pN, which is a challenge for direct measuring. One possible approach is to use atomic force microscopy (AFM) which can be sensitive enough for pN, but keeping the relative position of the two split rings and reducing the equipment drift will be tricky.

Here we propose a MEMS device to measure the force. This device contains a nanoscale cantilever, which is used to support one of the split ring pairs. The other split ring sits on the other substrate. The displacement of the cantilever is therefore proportional to the force between two plasmonic resonators. Figure 4.2 shows the schematic illustration of the device:

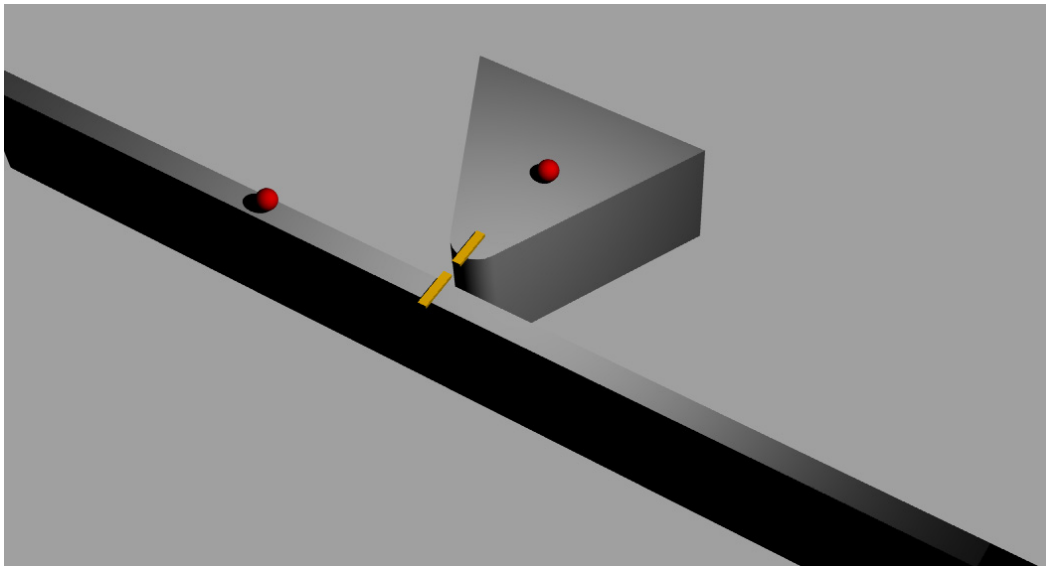

Figure 4.2 Schematic illustration of using cantilever for measuring optical force between plasmonic resonators. One of the plasmonic resonators sits on the nanoscale cantilever, and the other one is fixed on the substrate. The two red spheres can be two quantum dots, which are used to indicate the accurate position of the cantilever. Laser beam comes in from the top to generate the plasmonic trapping force, and drive the cantilever to move. The displacement of the cantilever can be derived by fitting the center of the quantum dots. In our experiment we used plasmonic split rings instead of the bowties, and we are not using quantum dots but the cantilever itself for the fitting.

There are many methods to accurately measure the displacement of a cantilever. Position Sensitive Detector (PSD) is widely used in every AFM setup to measure the tiny displacement of the AFM tip. Optical interferometry is also well established in the transduction of nanomechanical displacement[67]. Accurate determination of the capacitance between the cantilever and the substrates also demonstrates its capability in measuring the displacement[68]. In our experiment, we prove the possibility to measure the tiny displacement by using localization technique.

Localization technique has been used largely in the study of tracking a particle and Stimulated Emission Depletion (STED) microscopy[69]. It provides a way to break the diffraction limit, which is commonly at about $\lambda/2 \approx 250\text{nm}$. Any particle that is smaller than this dimension appears only a diffraction-limited bright spot in the microscope. Although any details within that bright spot cannot be distinguished in the microscope, the center of the spot and thus the location of the particle, can be determined very precisely, and can be expressed by the equation:

$$< (\Delta x)^2 >= \frac{s^2 + a^2/12}{N} + \frac{4\sqrt{\pi} s^3 b^2}{aN^2}$$

Here a is the width of pixels in CCD, s is the standard deviation of the point-spread function (Gaussian or otherwise), and N is the number of photons collected. This equation includes limiting cases of photon counting noise, pixilation nose and background noise. It also points out that by collecting a large amount of photons, the accuracy of the measurement can be extremely precise.

In our experiment, we use nanoscale cantilevers as the line source for the Gaussian fitting. When its width is much shorter than the wavelength (~ 500 nm), a cantilever can be considered as a perfect line source and forms one-dimensional Gaussian distribution in the image plane. By fitting the center of the line, we can determine the position within an error of merely 0.3 nm.

4.2 Fabrication Procedure

The whole structure is fabricated on a silicon-on-insulator (SOI) wafer. The thickness of the silicon layer is 250 nm, and box oxide is 3 μm. Firstly, a thin layer of PMMA is spin coated on the substrate (PMMA A3, 4000 rpm). Electron beam lithography is then used to define the cantilevers, stages and electrode pads on the PMMA. The width of the

cantilever is 50 nm, with a length of 100 μm. After develop the sample, a thin layer of SiO2 is then deposited by electron-beam thermal evaporation to form a mask. Deep reactive-ion etching (DRIE) is then applied to remove the silicon, leaving only the cantilever, stages and electrodes sitting on the substrate. The next step is to put the split ring pairs on the cantilever and substrate. Since the split rings are also prepared by e-beam lithography, this requires very accurate alignment between the two exposures, to accurately set the split rings on top of the cantilever. It was the bottleneck that reduces the yield for the old lithography system. But now the yield is higher. After the e-beam lithography, 2 nm Cr and 30 nm Au are then deposited to form the split rings.

After all structures are prepared, HF vapor etching is used to release the cantilever from the SiO2 substrate. Although BHF is more widely used for releasing and has advantages like better etch rate controlling, the nanoscale cantilever is very fragile in the solution and even slight vibrations may break it. Therefore HF vapor etching is recommended. After the cantilevers and substrates are connected to electrodes through wire binding, the sample is ready for measurement.

Figure 4.3 shows the SEM pictures of the device. The inset at the top-left is the overview of the device after packaged. A thin cover glass, which is hard to be seen in the photo, is used to cover the carrier chip. This cover glass can efficiently reduce the air flow which may be induced by the heating of the microscope, and help to stabilize the cantilever. In the center of Figure 4.3 is the overview of the cantilever, where you may see that the cantilevers are connected to one electrode, while the stage is connected to the other. Those electrodes can apply bias voltage between the sample and the stage, and the static electric force can pull the cantilever towards the stage. In this way we can control the distance between them.

The top-right inset shows the zoom-in region in the overview, and the bottom-right is even closer view of the stage tip and the cantilever. The fork like structure is the Au split ring, with the other split ring sitting on the corresponding position on the cantilever. The original separation between the two split rings is set to be 300 nm. This is because that during the HF vapor etching step, since the cantilever is very soft, it sometime can be stuck to the substrate. We found that preset the distance to be 300 nm can efficiently separate them.

The sample is then mounted on a dark-field microscope. Bias voltages are applied to vary the separation between split rings. The microscope magnifies the image 100 times and sends into a Hamamatsu camera for analysis.

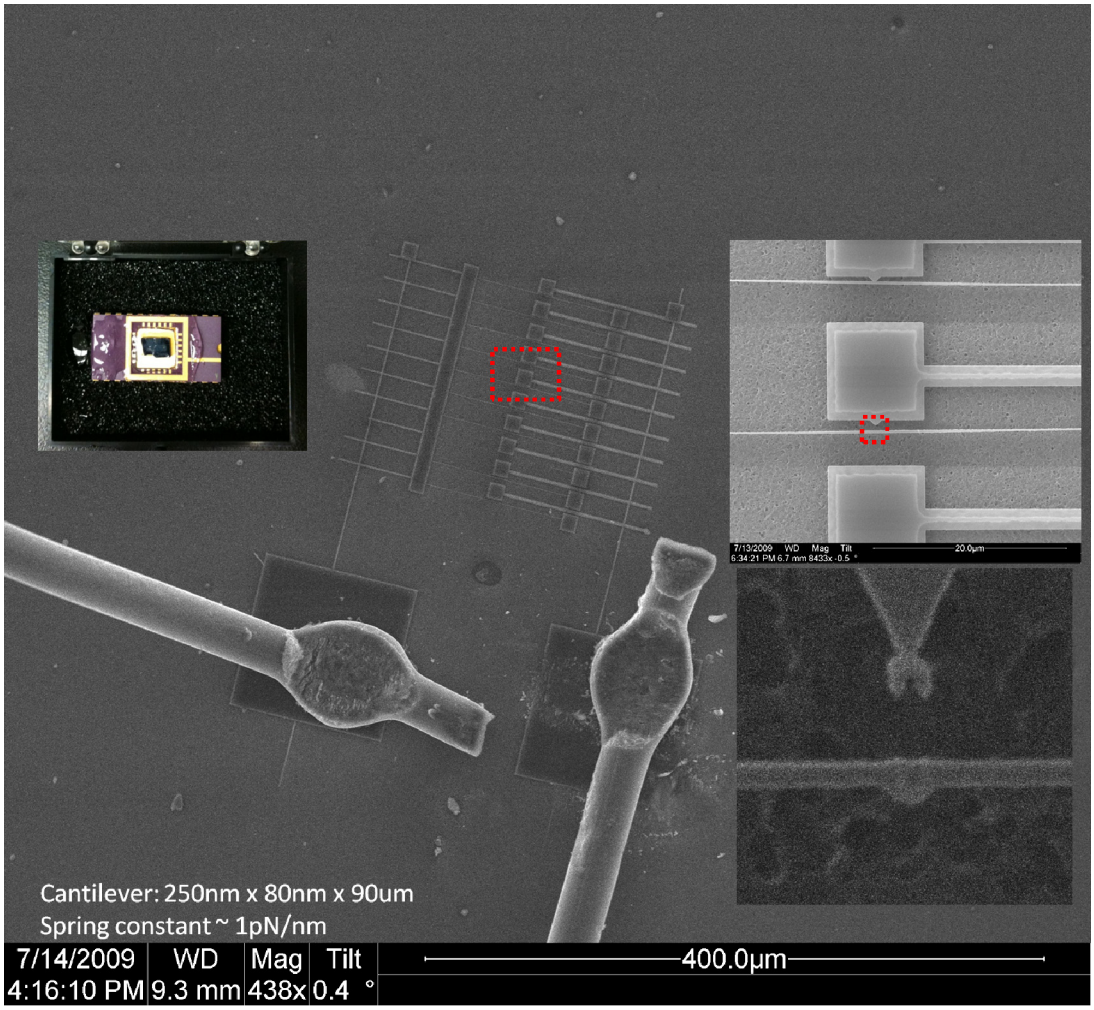

Figure 4.3 SEM pictures of the sample. The top-left inset is the overview of the sample with chip carrier. Middle, overview of the sample. Cantilevers are connected with one electrode, and the stages are connected with the other one. Top right, zoom-in view of the cantilever. Bottom right, zoom-in of the stage tip and the cantilever. The fork-like shape at the stage tip is a gold split ring, and its rival resonator is sitting at the corresponding position on the cantilever. The preset distance between the two split rings is 300 nm, and the static electric force between the stage and the cantilever can help to change this distance to the interested range.

4.3 Experiment Results (Preliminary)

Here we have only preliminary results, which show that this method is very promising for measuring forces at the order of 0.1 pN. Because of time issue, we are not measuring the force with it.

Figure 4.4 is a typical CCD image taken by the Hamamatsu camera. To reduce the background noise, a polarizer filter is added before the CCD camera, with the polarization axis the same along the cantilever. The digital gain in the camera is set to the lowest, because digital gain will not help to increase the accuracy but introduce extra noises. The low gain leads to an imaging rate of merely 5 frames per seconds.

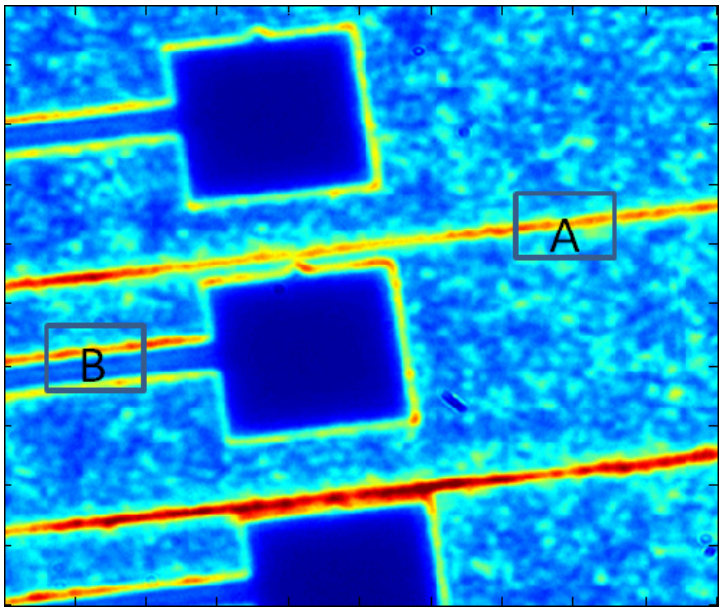

Figure 4.4 Optical images taken by a dark-field microscopy. A and B boxes indicate the two regions for data analysis. Region A is the cantilever, which moves towards region B when the static bias is applied. Region B is much wider than the cantilever and is considered to be stable, therefore it can be considered as a reference point in the Gaussian fitting. To increase the accuracy, we used a polarizer to increase the contrast between the cantilever and the background noise.

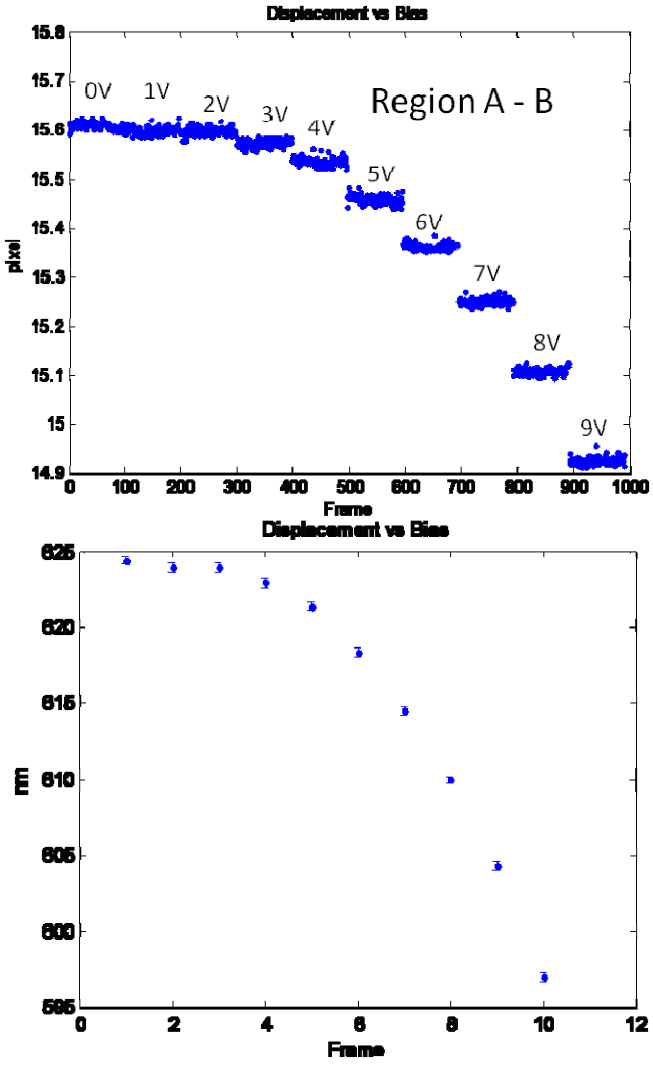

Figure 4.5 Displacement of the cantilever under different static bias. Top, fitting results for the relative distance between region A and region B, in unit of pixel number. At each voltage, 100 images were taken. Bottom, averaged position with error bars, in nanometers.

Both cantilevers and stages are shown clearly in the image. We took a short range (~ 3 μm) of the cantilever for fitting one dimensional Gaussian distribution. Then another region B, on the edge of the stage, is taken as reference point. This reference point is not needed for fast measurement. However it is critical for long term imaging, to cancel out the drifting effect of the stage.

Figure 4.5 shows the fitting results for a series of images. The bias voltage is changed from 0 V to 9 V to pull the cantilever closer to the stage, and at each bias voltage, 100 images are taken for measuring. For the present design, 9 volts can shift the cantilever for about 30 nm. For better control of the cantilever, a larger stage is required.

Figure 4.6 shows the standard deviation of each 100-counting images. An average resolution 0.3 nm is achieved with our setup.

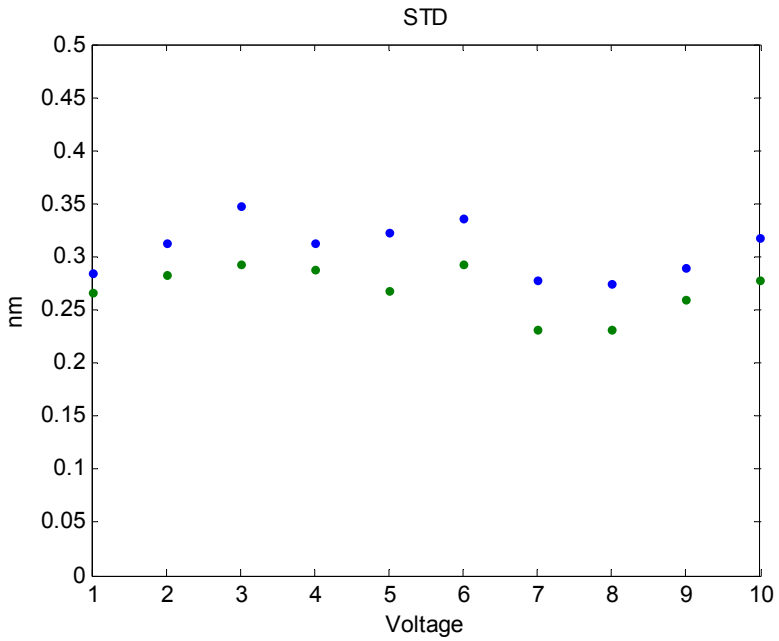

Figure 4.6 Standard deviation of the cantilever positions. 0.3 nm resolution has been achieved with our present setup.

The cantilevers have both ends fixed on the substrate. Therefore its spring constant can be calculated from the cantilever dimensions and material constants:

$$k = \frac{192EI}{L^3} = 16\frac{Ew^3h}{L^3}$$

Here w is the width of the cantilever, h is the height, and L is the length. For a cantilever with w=100 nm, h= 250 nm, and L= 100μm, the spring constant is 1 mN/m, which equals to 1 pN/nm. In this case, the cantilever used in our experiment has the capability to measure sub pico-Newton forces.

By reducing the background noises, we believe that we can improve the resolution for one order.

To conclude, we calculate the optical force between two plasmonic resonators, and design a cantilever-based MEMS setup for measuring this force. The new approach allows us to have a very high resolution for the cantilever, and therefore sub-pico-Newton can be measured.

Chapter 5

Graphene-based Broadband Optical Modulator

The aim of this chapter is to demonstrate a new type of optical modulator based on graphene, which contains only a monolayer of carbon atoms. We use graphene as the active layer in an optical modulator and demonstrate its outstanding performances compared with other products.

5.1 Background introduction

5.1.1 Modulators: General Overview

Telecommunications and on-chip interconnects are reaching a bottle-neck for the speed. Modern semiconductor fabrication technology has kept shrinking the sizes and increasing the speed of the transistors, doubles for every 18 months. But the metal interconnects are not following at the same rate. As the semiconductor industry has been blow the 150 nm node, interconnect RC delay has caused signal desynchronization and increased bit error rates.

Integration of photonics and microelectronics provides a promising solution to solve the communication problem. Optical interconnectors can bring several advantages compared with their electrical counterpart. For example, they may improve the separation of electric devices, and therefore optimize the chip layout for better temperature control while without reducing operation rates. They may also help to reduce the energy consumptions on the chip, because for now interconnects are consuming 80% of the processor's power.

The goal for photonics devices would be silicon-based optoelectronics where they may meet and seamlessly cooperate with electronics intelligence. And among all the optoelectronic devices, modulator is one of the main required functionalities for the interconnectors. Compared with directly modulating the light source, an external modulation offers several advantages. It is usually more economic than modulating light source, and the speed can be higher. And the most important, one light source can drive multiple channels through different modulators, without influencing each other while

reducing the total power consumption.

A modulator is designed to modulate the characteristics of light, either in free space or in a waveguide. Several physics mechanisms can be used for this purpose, to change different parameters such as intensity, phase or polarizations. Depending on the parameters they change, modulators can be categorized as either electro-refractive or electro-absorptive.

An electro-refractive (ER) modulator changes the real part of refractive index with the applied electric field, while an electro-absorptive (EA) modulator changes the imaginary part. Among all the practical methods, the most common way is utilizing the plasma dispersion effect, which is represented by the free carriers in the semiconductor. It has been proven by Soref and Bennett that at a wavelength of 1.55 μm, the change of refractive index can be expressed by equations:

$$\Delta n = \Delta n_e + \Delta n_h = -(8.8\times10^{-22}\times\Delta N_e + 8.5\times10^{-18}\times(\Delta N_h)^{0.8})$$
$$\Delta\alpha = \Delta\alpha_e + \Delta\alpha_h = 8.5\times10^{-18}\times\Delta N_e + 6\times10^{-18}\times\Delta N_h$$

Here Δn is the change of real part in refractive index, and $\Delta\alpha$ is the imaginary part of it. Both Δn and $\Delta\alpha$ are related to the change of free-electrons and free-holes concentrations. Similar equations with slightly different coefficients can be used for the wavelength of 1.3 μm.

From these equations we can easily estimate the change of refractive index in the semiconductor. For example, when the carrier density changes 1×10^{18} cm^{-3}, the real part of the refractive index changes -3.3×10^{-3} for the operation wavelength of 1.55 μm, and the imaginary part is the similar order.

The imaginary part of the refractive index is directly related to the loss in the propagation. And obviously that it can be used to modulate the intensity of the propagating mode. However, the influence from the real part is not so directly. In the propagation equations, real part of the refractive index cannot change the intensity of the light, but only add extra phases to it. Base on this phase change, there are two essential options available for the modulators. First, this extra phase can change the resonance conditions in an optical cavity, thus allows the device to be turned on and off at the given wavelength. Second, for two propagating waves, if the phase is changed for one of them, the interference between them can be changed, either constructive or destructive. Typically, a Mach-Zehnder interferometer (MZI) is widely used, based on this mechanism.

As we have estimated, the change of the refractive index is very small, and the relative change of $\Delta n / n$ is usually at the order of 10^{-4}. This means that after the light propagates a distance of one wavelength, its phase can be modified by merely 10^{-4}, and the phase shift in the optical mode can be given by:

$$\Delta\phi = \frac{2\pi}{\lambda}\Delta n \cdot L$$

Here λ is the wavelength of the light, and L is the length of the device. Therefore, to accumulate enough phase change, a long propagating distance is generally required for MZI. For example, the first demonstrated silicon-based MZI has a footprint up to 8 mm[70].

Recently, alternative attempts have been tried on other materials, such as germanium and SiGe, which may potentially compatible with silicon industry. Those materials may have strong Franz-Keldysh effect or quantum-confined Stark effect (QCSE) where electric field may induce optical absorption.

So far we have briefly introduced the mechanisms for the optical modulators. But they are also facing their own challenges. For instance, semiconductor modulators have witnessed rapidly-expanding research interests over the past half decade; however, the device footprint of silicon-based modulators are on the order of millimeters, limited by its weak plasma dispersion[70]. Germanium and compound semiconductors, on the other hand, face the major challenge of integration with existing electronics and photonics platforms[71-73]. High quality-factor optical resonators have been used to increase the modulation strength, however, these devices suffer from intrinsic narrow-bandwidth aside from their sophisticated optical design and stringent fabrication tolerance[74]. Finding a CMOS compatible material with adequate modulation speed and strength is becoming a task of not only scientific interest, but also industrial significance.

We here propose and demonstrate that graphene may be a promising candidate for a modulator which includes all the merits: high speed, small footprint, broadband and inert to thermal effect.

5.1.2 Graphene: monolayer of carbon atoms

Graphene, formed by a single layer of carbon atoms in a hexagonal lattice, has attracted great interest because of its exceptional optical and electrical properties[75-79]. The linear dispersion of graphene allows direct coupling between light and relativistic electrons,

resulting in frequency independent optical absorption for a broad spectral range from visible to infrared[80,81]. The overall absorption of layered graphene is proportional to the number of layers, each absorbing $\pi\alpha = 2.293\%$, where α is the fine-structure constant ($\frac{e^2}{\hbar c}$). Moreover, the resonant interband absorption of graphene can be widely tuned by adjusting the Fermi level of Dirac electrons through a gating electric field perpendicular to the graphene sheet[82].

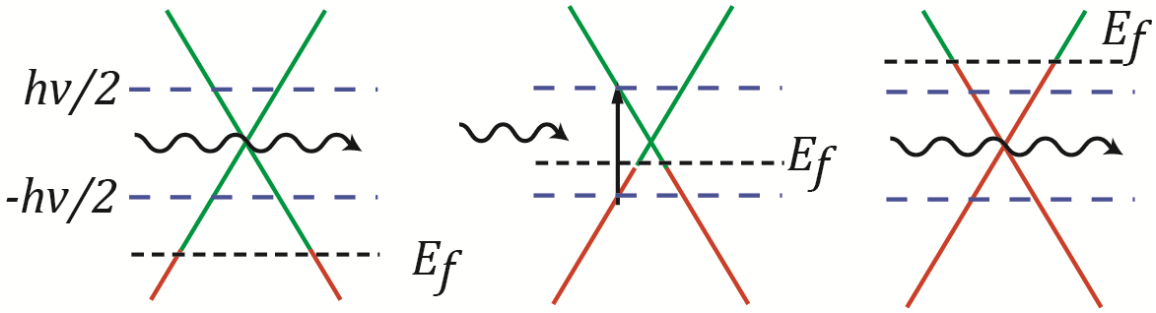

Figure 5.1 Band structure of graphene, under gating electric field. Formed by only monolayer of carbon atoms, the graphene has very low density of states. Therefore the surface charges can efficiently shift the Fermi levels and then change the absorption of the material. Left, when the graphene is charged by positive charges, the Fermi level is lowered. There is no electron available for the interband transition. Middle, bias voltage is low. The incident light can excite the electrons. Right, when the graphene is negatively charged, the Fermi level is higher than half of the photon energy, there is no state available for the electrons to be excited to. Therefore the ideal absorption in this case is zero.

Figure 5.1 shows the band structure of the graphene, under different gating bias. Ideal graphene has linear band structure near the Fermi level, and has a zero band gap. Because the graphene is formed by monolayer of carbon, its density of state (DOS) is very low compared with bulk materials. Therefore even small charge accumulation can effectively shift the position of the Fermi level. When the graphene is charged by positive charges, the Fermi level is lowered. There is no electron available for the interband transition, and thereby the absorption of the material is zero. If the graphene is not charged, the Fermi level is in the middle of the band structure, close to the Dirac point. The incident light can excite the electrons. When the graphene is negatively charged, the Fermi level is higher than half of the photon energy, there is no state

available for the electrons to be excited to. Therefore the ideal absorption in this case is zero again.

Such a strong electroabsorption (EA) effect, which has not yet been observed in bulk materials, originates from the 2D lattice structure and implies the potential for graphene to be used as the active medium in an EA modulator. In comparison to compound semiconductors such as GaAs and quantum-well with quantum-confined Stark effect (QCSE), a monolayer graphene possesses a much stronger resonant interband optical transition, resulting in novel optoelectronic devices such as graphene lasers[83] and photoreceivers[84,85].

The vanishing of effective mass and high Fermi velocity of carriers in graphene makes it a promising candidate for post-silicon electronics, particularly for high frequency applications[86,87]. With the carrier mobility exceeding 200,000 $cm^2 V^{-1} s^{-1}$ at room temperature[88,89], among the highest in all known materials, the Fermi level and hence the optical absorptions of graphene can be rapidly modulated through band-filling effect. In addition, the speed limiting processes such as the photocarrier generation and relaxation in graphene are on the timescale of picoseconds and can support opto-electronic devices upto 500 GHz[90], depending on the carrier density and graphene quality. Here we report the first waveguide integrated graphene EA modulator by actively tuning the Fermi level of a monolayer graphene sheet. The gigahertz graphene modulator demonstrates a strong EA modulation of 0.1dB/um and operates over a broad range of wavelength from 1350 nm to 1600 nm. As the graphene technology is compatible with conventional Complementary Metal-Oxide-Semiconductor (CMOS) processing, monolithic integration of the graphene EA modulator opens new routes to integrated photonics due to its combined advantages of compact footprint, low voltage operation and ultrafast modulation across a broad range of wavelengths.

5.2 Experiment Design

When the light propagates perpendicularly through a monolayer graphene, the absorption is 2.3%, which is far too low for a modulator. One solution is using multiple layers, and the total absorption will be proportional to the layer numbers. The other way is to let the light propagate along the graphene, where the black material may absorb more light. This is the basic idea we are using for our device.

The graphene is metallic layer, so it cannot support an optical mode directly. Meanwhile, since the electron density is so low, although it can support a surface plasmon mode, it

can only work at tera-Herz frequency. To let the light propagate along the graphene, a waveguide must be integrated.

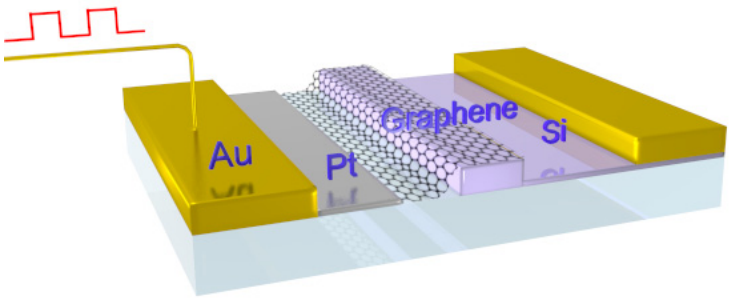

Figure 5.2 Graphene-based silicon-integrated optical modulator. Three dimensional schematic illustration of the device, with a monolayer graphene sheet on the top of a bus silicon waveguide and a 7-nm-thick Al2O3 in between as a gate oxide. The silicon waveguide is connected to the electrode through a 50-nm-thick p-doped silicon layer. The graphene is overlapped by a 10-nm-thick platinum to reduce the resistance.

Figure 5.2 shows the illustration of the final device. A silicon bus waveguide is used to conduct the light. A graphene layer is laid on the waveguide, with a thin layer of aluminum oxide in between. The graphene and the waveguide are contacted to different electrodes, for the bias voltage. When the bias voltage is added, the electric field will be formed between the graphene and the silicon waveguide, and the electrons accumulated on the graphene will shift the Fermi level and thereby change the absorption coefficient.

As we all know, although the light is confined by the silicon waveguide, it still has

electric and magnetic fields penetrating outside of the waveguide, known as the evanescent wave. To maximize the electric field component in the evanescent wave is directly related to the device performance.

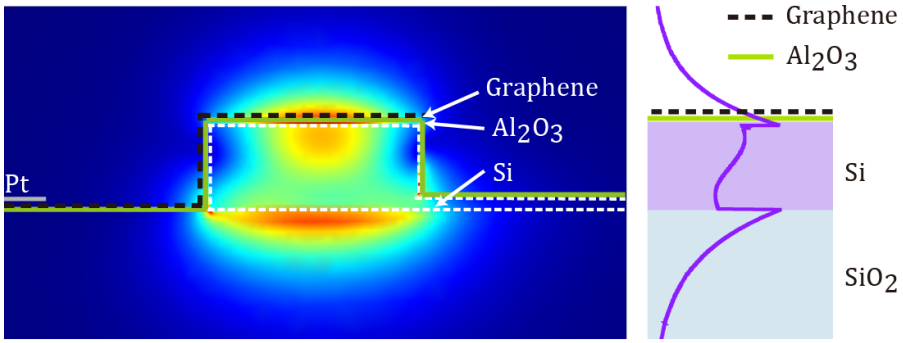

Figure 5.3 Optical mode for the device. The silicon waveguide, 600 nm in width and 250 nm in height for the cross section, can support multiple modes. We choose the second mode, which has the electric field maximum at the top and bottom surface of the waveguide, as shown by the blue curve in the left panel. From the COMSOL simulation result, we can also see that the thin platinum electrode and the 50-nm-thick silicon layer have negligible influence to the mode shape. The Pt is 10 nm thick and 500 nm away from the waveguide. The actual thicknesses of graphene sheet and Al_2O_3 in the simulation are 0.7 nm and 7 nm, respectively.

Figure 5.3 shows the optical mode we choose for the device. Since our waveguide cross section, 600 nm in width and 250 nm in height, is much larger than the cut-off cross section, the waveguide we use can support multiple modes. This allows us to choose the proper mode, which has the electric field maximum at the top and bottom surface of the waveguide, as shown by the blue curve in the left panel. We used COMSOL for the simulation. From the simulation, we can also confirm that the platinum electrode and the 50-nm-thick silicon layer have negligible perturbations to the optical mode.

5.3 Fabrication Procedure

The graphene-based modulator is prepared on a silicon-on-insulator (SOI) wafer. First, waveguides are prepared by standard e-beam lithography and deep reactive-ion etching (DRIE). Then a thin layer of aluminum oxide (7 nm) is prepared by atom layer deposition (ALD). The graphene prepared by standard chemical vapor deposition (CVD) method is then transferred to the chip, covering all devices. After the electrode is defined, a thin layer of PMMA is used to protect the graphene on the top of the waveguide and between Pt and the waveguide. And the rest graphene is removed by oxygen plasma.

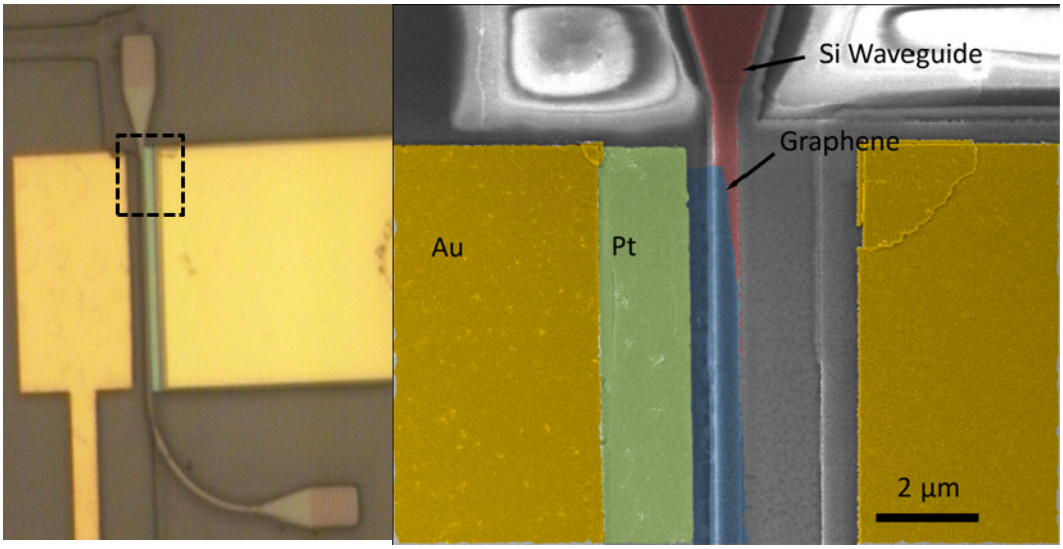

Figure 5.4 Optical microscopic and SEM images of the fabricated device. a, Top-view microscope image of the waveguide, with the dashed region shown by a SEM image in **b**. False colors are used to illustrate Au electrode (Yellow), Pt electrode (Green), graphene sheet (blue) and waveguide (red). The width of the Si waveguide is 600 nm, while the gap between the Pt electrode and the Si waveguide is 500 nm. The bright multi-ring region beside the Au electrodes is due to charging effect on the SiO_2 layer in the SEM.

Figure 5.4 shows the optical microscope picture and SEM images. To couple the laser from the free space to the waveguide, we use grating couplers. The advantage of the grating coupler is that it can couple the light to the mode we need, which is shown in Figure 5.3. However, the intrinsic loss of the device is also mainly contributed by the grating coupler. To get better performance, further designs such as shallow gratings

should be considered in the future.

In the device, the bus waveguide is bended for 90 degrees, to change the polarization of the incident light from the outgoing light. In this way, we can easily separate the two beams by using a polarizer and the signal-to-noise ration can be improved.

5.4 Static Response

Before we characterize the high frequency performance of the device, we measure the transmission with static bias voltage.

5.4.1 Single wavelength

The static response of the device at 1550 nm is dependent on the gate voltage and can be divided in three regions, as shown in Fig. 5.5. At low gate voltage (-1 V<V<*3.8*V), the Fermi level $E_f(V)$ of graphene is close to the Dirac point ($\left|E_f(V)\right| < \hbar\omega_0 / 2$), and interband transitions occur when electrons are excited by the 1550 nm incoming photons ($\hbar\omega_0$). The optical absorption of graphene is determined by the position of the Fermi level. By adding a bias between the graphene and the waveguide, we can tune the Fermi level of graphene, and therefore modulate the total transmission. With the current waveguide design, the modulation depth is as high as 0.1dB/um, resulting in a graphene EA modulator with a footprint of merely 25 μm^2. At large negative V (<-1V), the Fermi level is lowered below the transition threshold ($\left|E_f(V)\right| = \hbar\omega_0 / 2$) due to positive charge accumulation. As a result, there would be no electron available for interband transition, and hence the graphene would appear transparent. On the other hand, at large positive gate voltage (>3.8V), all the electron states are filled up, and no interband transition is allowed. Ideally, there should be a sharp change in transmission at $\left|E_f(V)\right| = \hbar\omega_0 / 2$. In reality, this transition was broadened owing to the defects in graphene[91], and shifted to higher V due to natural doping from the substrate.

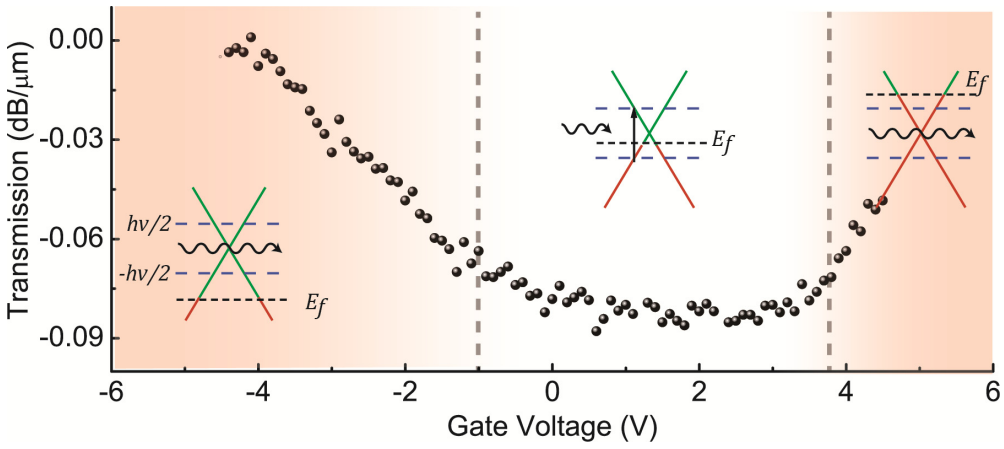

Figure 5.5 DC measurement of the modulator. The main panel shows the modulation depth, normalized to the device length (40 μm), under different gate voltage (V_g). Three regions can be found in the figure. In the middle region with V_g from -1 V to 3.8 V, the Fermi level is close to the Dirac point and the interband transition is allowed. Thus the graphene sheet is absorptive. When V_g < -1 V, the Fermi level is lowered and there is no electrons available for interband transition. While when V_g >3.8 V, all electron states in resonant with *hv* are occupied, and the transition is forbidden. In both of the later two cases, the transmission increases.

5.4.2 Broadband Performance

As the overall optical opacity of graphene is independent of wavelength and the high frequency dynamic conductivity for Dirac fermions is a constant, the graphene EA modulator is therefore intrinsically broadband, unlike modulators based on optical cavities[74] or resonant optical effects such as QSEC[71]. In order to access this broadband effect, we use white light source from a supercontinuous laser. The gate dependent 2D spectra of the EA modulator are shown in Fig. 5.6. A 3dB modulation is achieved for a broadband wavelength from 1350 nm to 1600 nm with a gate voltage of -5 V. Although a higher modulation depth and broader wavelength range are expected at a higher gate voltage, we chose to use low gate voltage not only to avoid gate oxide breakdown but also because high driving voltages increases power assumptions and violates voltage restrictions in CMOS process.

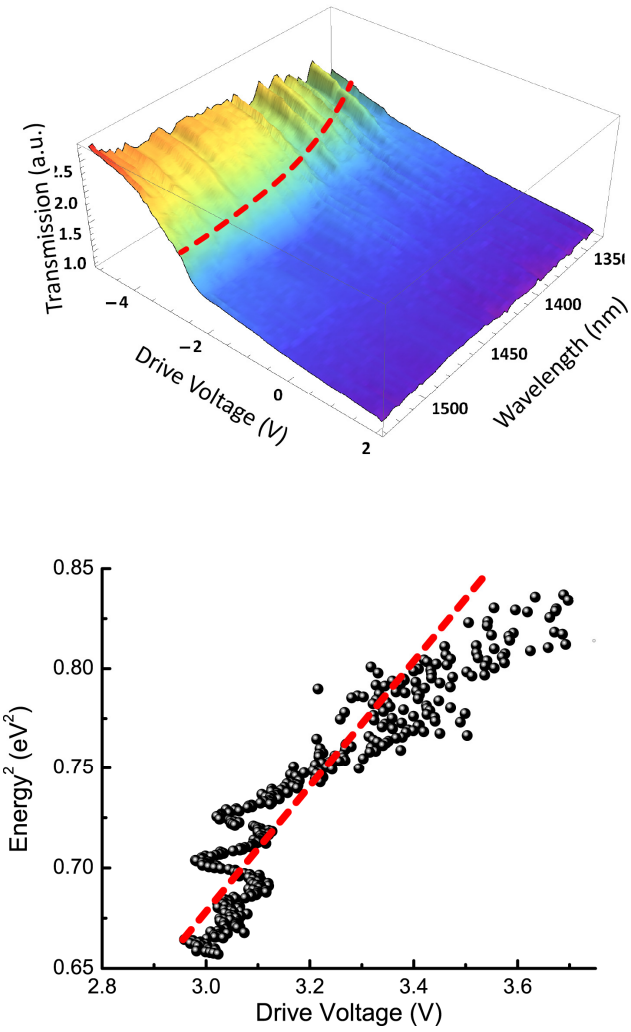

Figure 5.6 Spectrum characterization of the optical modulator. a, The transmission of the device with different gate voltage, ranging from 1350 nm to 1600 nm. The transmission is normalized to V_g = 1 V. The red dashed curve shows the rough position of transmission equal to 1.5, which unambiguously bends to higher gate voltage at shorter wavelengths. **b**, the trace of the modulation voltage plotted as squared photon energy versus gate voltage. The red dashed line shows the linear fitting to the experimental data, which directly yields the Fermi velocity of $v_f = 0.9 \times 10^6 m/s$.

The 2D transmission spectra also allow us to determine the electronic band dispersion of the CVD grown graphene. As the Graphene EA modulation is dictated by the optical transition, $\hbar\omega = 2|E_f|$, the graphene modulator has different response at different wavelengths. Higher photon energy always requires larger change in the Fermi level. The trace for maximum transmission change, shown as dashed line in Fig. 5.6, is defined by $\hbar\omega = 2E_f = 2\hbar v_F\sqrt{\alpha\pi|V+V_0|}$, where v_F is the Fermi velocity, V and V_0 are the gate voltage and the voltage offset caused by natural doping, respectively. $\alpha = 8.7\times10^{16}\,m^{-1}V^{-1}$, as estimated from a capacitor model. The gate voltage dependent transition frequency is plotted in Fig. 5b, in which $\hbar\omega = 558meV\sqrt{|V+V_0|}$. The linear fit determines the voltage offset of -0.8 V and the Fermi velocity of 0.8×10^6 m/s, which agrees with other researches[92,93].

5.5 Dynamic Response

To measure the dynamic response of the graphene modulator, radio frequency (RF) signals generated by a network analyzer was added on a static V_D and applied to the modulator. The same 1.53 μm laser was used to test the modulator, and the out-coupled light was sent to a high-speed photodetector. Shown in Fig. 5.7 are the V_D dependant RF responses of the graphene modulator, showing gigahertz operation of the device at various drive voltages. Owing to the exceptionally high carrier mobility and saturation velocity of graphene, the bandwidth is not limited by the carrier transit time, but by the parasitic response of the device. With the platinum electrode placed 500 nm away from the waveguide, the total resistance of the system is reduced to around several hundred ohms. This resistance, together with the capacitance on the order of 0.5 pF, limits the operation bandwidth of the present device to giga-hertz.

The 3dB modulation bandwidth is independent to the V_D while the modulation efficiency is not. The device response at low frequency (300 kHz) is shown in the inset of Fig. 5.7. At low V_D, the modulation response is weak as the optical transmission is insensitive to V_D. When the drive voltage is increased, the RF response increases to maximum at V_D = -4 V. As the drive voltage increases further, the modulation efficiency saturates as graphene is transparent within the modulation range of the bias voltage.

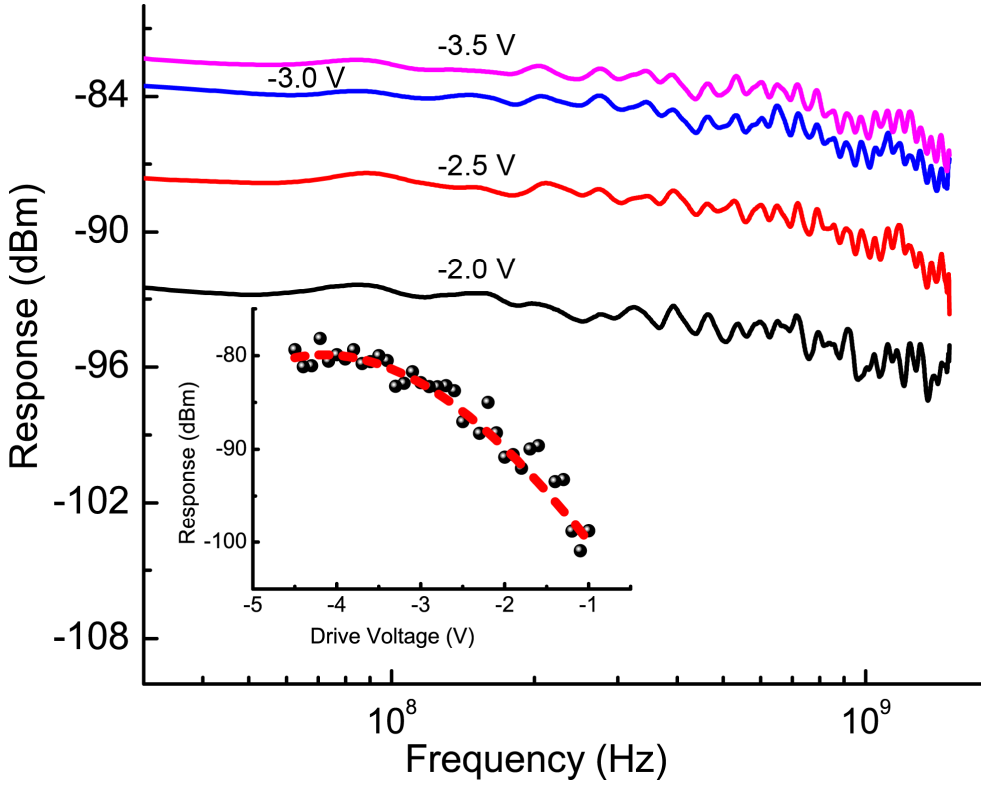

Figure 5.7 Electro-optics response of the device. The measured 3 dB bandwidth of the device are found at 0.8 GHz, 1.1 GHz, 1.1 GHz and 1.2 GHz, for the drive voltages of -2.0 V, -2.5 V, -3.0 V and -3.5 V, respectively. The bandwidths are mainly restricted by the parasitic response of the device. The inset shows the response at static, indicating that the device has the best performance at drive voltage of -4V. The laser wavelength is 1.53 μm in the test.

To conclude, we demonstrated that the graphene-based optical modulator has exhibited broad optical bandwidth (1.35-1.6 μm), small device footprint (25μm^2), and high operation speed (1.2 GHz at 3dB) under ambient conditions, all of which are essential for optical interconnects for future integrated opto-electronic systems. The modulation efficiency of a single layer of hexagonal carbon atom is already comparable to, if not better than, traditional semiconductor materials such as Si, GeSi and InGaAs, which are orders of magnitude larger in active volume. By incorporating multi-layer graphene sheets, the modulation efficiency can be increased even further. The flexibility of

graphene sheets could also enable radically different photonic devices. For example, it can be integrated with flexible substrate and plastic waveguides[94]. Or it could be used in novel geometries such as core-shell modulator of nano-optical cable. The recent development of large scale graphene synthesis and transfer techniques[95] ensure its comparability with the existing integrated electronics platform.

Chapter 6

Summary and Future Directions

6.1 Summary

Novel optical devices, including plasmon-enhanced light-mill and graphene-based optical modulator, are discussed in this dissertation. Both devices have not only interesting physics mechanisms behind them, but also potential applications in broad fields, including biological sample manipulation and information communication.

In the plasmon-enhanced light-mill section, both intuitive explanations based on Poynting vectors and strict characterizations are carried out by using full-wave vectorial simulations. Surface plasmon enhancing effect is found as the torque is maximized at the plasmon resonance frequencies, indicating that plasmonic effect may help to shrink the size of the actuator device without losing its power. Another out-of-expectation result is that the torque has different directions for different plasmonic resonance modes, which provides extra freedom for control in future applications.

To demonstrate its exceptional performance, we encapsulate the light-mill inside a dielectric disk which is 4,000 times larger in volume. The dielectric disk can be regarded as a heavy duty for the light-mill to drive in liquid. By using dark field microscopy, we demonstrate that at resonant frequency single light-mill can generate enough torque for rotating the disk. With multiple light-mills integrated into one dielectric disk, we also mapped the rotation speeds around both resonant frequencies. The magnitude of the torque is evaluated to be around 140 pN·nm with an incident light intensity of $1 mW/\mu m^2$. This torque may find its applications as actuators to drive NEMS or wind/unwind DNAs.

The design and fabrication of silicon cantilevers for measuring the interaction between plasmonic resonators are also demonstrated. These cantilevers are mechanically robust and flexible and can be very sensitive to the forces carried out by the plasmonic structures which are fixed to the cantilevers. Meanwhile, the displacement of these cantilevers can be precisely measured by using localization technology. A precision of 0.3 nm can be achieved with present design, which means the setup is readily adaptable for measuring sub-pN force.

In the second section of this dissertation, the first graphene-based Si-waveguide integrated broadband optical modulator is demonstrated. Although it has only one layer of carbon atoms, graphene provides outstanding modulation efficiency (0.1 dB/μm) when placed on top of a Si waveguide. This allows the small footprint (25 μm^2) for the device and is adaptable for the requirement in integration. Speed test is also performed on the device, and 1.2 GHz modulation speed is achieved with current design, which is only limited by the RC constant of the device. The broadband (1.35 ~ 1.6 μm) response of the device enables it to cover all the communication wavelengths. All of these features, small footprint, high modulation efficiency, broadband, high speed and athermal modulation, make the graphene-based modulator tackles the long standing problem to shrink photonics into chip-scale.

6.2 Future directions

6.2.1 Aharmonic lateral force on split ring resonator

Optical rectification effect always accompanies with second harmonic generations (SHG). Although nonlinear processes like SHG or high-order harmonic generations have been demonstrated on plasmonic structures, optical rectification has hardly been addressed yet. Optical rectification on the plasmonic structures has the same effect as a lateral force, which is called aharmonic force. The study of the aharmonic force on plasmonic structures may help to understand the nonlinear process and may also lead to new design of linear actuators.

6.2.2 Plasmonic-integrated graphene-based optical modulator

To integrate it on chip, both the footprint and speed of the modulator is critical. The present modulator is limited by the cross-section of the Si waveguide, which requires a few hundred nanometers in width and tens of microns in length. Plasmonic waveguide may improve this since it can enhance the electric field of the electromagnetic wave, and therefore high modulation efficiency is expected. Since the diameter of a plasmonic waveguide can be less than 100 nm, the modulation speed can be faster because both the resistance and capacitance of the system are smaller.

Reference

1 Crookes, W. Attraction and repulsion caused by radiation. *Nature* **12**, 125, (1875).

2 Jain, P. K. & El-Sayed, M. A. Universal scaling of plasmon coupling in metal nanostructures: Extension from particle pairs to nanoshells. *Nano Letters* **7**, 2854-2858, (2007).

3 Reynolds, O. On certain dimensional properties of matter in the gaseous state. Part II. *Philosophical Transactions of the Royal Society of London* **170**, 727-845, (1879).

4 Pfeifer, R., Nieminen, T., Heckenberg, N. & Rubinsztein-Dunlop, H. Colloquium: Momentum of an electromagnetic wave in dielectric media. *Reviews of Modern Physics* **79**, 1197-1216, (2007).

5 Lebedew, P. An experimental investigation of the pressure of light. *Astrophys J* **15**, 60-62, (1902).

6 Nichols, E. F. & Hull, G. F. A preliminary communication on the pressure of heat and light radiation. *Phys Rev* **13**, 307-320, (1901).

7 Nichols, E. F. & Hull, G. F. The pressure due to radiation. *Astrophys J* **17**, 315-351, (1903).

8 Ashkin, A., Dziedzic, J. M., Bjorkholm, J. E. & Chu, S. Observation of a Single-Beam Gradient Force Optical Trap for Dielectric Particles. *Opt Lett* **11**, 288-290, (1986).

9 Raab, E. L., Prentiss, M., Cable, A., Chu, S. & Pritchard, D. E. Trapping of Neutral Sodium Atoms with Radiation Pressure. *Phys Rev Lett* **59**, 2631-2634, (1987).

10 Ketterle, W. Nobel lecture: When atoms behave as waves: Bose-Einstein condensation and the atom laser. *Reviews of Modern Physics* **74**, 1131-1151, (2002).

Reference

11 Grier, D. G. A revolution in optical manipulation. *Nature* **424**, 810-816, (2003).

12 Povinelli, M. L., Johnson, S. G., Loncar, M., Ibanescu, M., Smythe, E. J., Capasso, F. & Joannopoulos, J. D. High-Q enhancement of attractive and repulsive optical forces between coupled whispering-gallery-mode resonators. *Opt Express* **13**, 8286-8295, (2005).

13 Dholakia, K., Reece, P. & Gu, M. Optical micromanipulation. *Chemical Society Reviews* **37**, 42-55, (2008).

14 Krapchev, V. B. Kinetic-Theory of the Ponderomotive Effects in a Plasma. *Phys Rev Lett* **42**, 497-500, (1979).

15 Teubner, U. & Gibbon, P. High-order harmonics from laser-irradiated plasma surfaces. *Reviews of Modern Physics* **81**, 445-479, (2009).

16 Beth, R. A. Mechanical detection and measurement of the angular momentum of light. *Phys Rev* **50**, 115-125, (1936).

17 Allen, L., Beijersbergen, M. W., Spreeuw, R. J. C. & Woerdman, J. P. Orbital Angular-Momentum of Light and the Transformation of Laguerre-Gaussian Laser Modes. *Phys Rev A* **45**, 8185-8189, (1992).

18 Padgett, M. J. & Allen, L. The angular momentum of light: optical spanners and the rotational frequency shift. *Opt Quant Electron* **31**, 1-12, (1999).

19 Paterson, L., MacDonald, M. P., Arlt, J., Sibbett, W., Bryant, P. E. & Dholakia, K. Controlled rotation of optically trapped microscopic particles. *Science* **292**, 912-914, (2001).

20 Gore, J., Bryant, Z., Nollmann, M., Le, M. U., Cozzarelli, N. R. & Bustamante, C. DNA overwinds when stretched. *Nature* **442**, 836-839, (2006).

21 Matsuo, S., Kiyama, S., Shichijo, Y., Tomita, T., Hashimoto, S., Hosokawa, Y. & Masuhara, H. Laser microfabrication and rotation of ship-in-a-bottle optical rotators. *Appl. Phys. Lett.* **93**, 051107, (2008).

22 He, H., Friese, M. E. J., Heckenberg, N. R. & Rubinszteindunlop, H. Direct

Observation of Transfer of Angular-Momentum to Absorptive Particles from a Laser-Beam with a Phase Singularity. *Phys Rev Lett* **75**, 826-829, (1995).

23 Friese, M. E. J., Nieminen, T. A., Heckenberg, N. R. & Rubinsztein-Dunlop, H. Optical alignment and spinning of laser-trapped microscopic particles. *Nature* **394**, 348-350, (1998).

24 Garces-Chavez, V., McGloin, D., Padgett, M. J., Dultz, W., Schmitzer, H. & Dholakia, K. Observation of the transfer of the local angular momentum density of a multiringed light beam to an optically trapped particle. *Phys Rev Lett* **91**, 093602, (2003).

25 Galajda, P. & Ormos, P. Complex micromachines produced and driven by light. *Appl. Phys. Lett.* **78**, 249-251, (2001).

26 Knoner, G., Parkin, S., Nieminen, T. A., Loke, V. L. Y., Heckenberg, N. R. & Rubinsztein-Dunlop, H. Integrated optomechanical microelements. *Opt Express* **15**, 5521-5530, (2007).

27 Sokolov, A., Apodaca, M. M., Grzybowski, B. A. & Aranson, I. S. Swimming bacteria power microscopic gears. *Proc. Natl. Acad. Sci. U. S. A.* **107**, 969-974, (2010).

28 Higurashi, E., Sawada, R. & Ito, T. Optically induced rotation of a trapped micro-object about an axis perpendicular to the laser beam axis. *Appl. Phys. Lett.* **72**, 2951-2953, (1998).

29 Astumian, R. D. Thermodynamics and kinetics of a Brownian motor. *Science* **276**, 917-922, (1997).

30 Barnes, W. L., Dereux, A. & Ebbesen, T. W. Surface plasmon subwavelength optics. *Nature* **424**, 824-830, (2003).

31 Bliokh, K. Y., Bliokh, Y. P., Freilikher, V., Savel'ev, S. & Nori, F. Colloquium: Unusual resonators: Plasmonics, metamaterials, and random media. *Reviews of Modern Physics* **80**, 1201-1213, (2008).

32 Fang, N., Lee, H., Sun, C. & Zhang, X. Sub-diffraction-limited optical imaging

with a silver superlens. *Science* **308**, 534-537, (2005).

33 Moskovits, M. Surface-Enhanced Spectroscopy. *Reviews of Modern Physics* **57**, 783-826, (1985).

34 Smith, D. R., Pendry, J. B. & Wiltshire, M. C. K. Metamaterials and negative refractive index. *Science* **305**, 788-792, (2004).

35 Falk, A. L., Koppens, F. H. L., Yu, C. L., Kang, K., Snapp, N. D., Akimov, A. V., Jo, M. H., Lukin, M. D. & Park, H. Near-field electrical detection of optical plasmons and single-plasmon sources. *Nature Physics* **5**, 475-479, (2009).

36 Hentschel, M., Saliba, M., Vogelgesang, R., Giessen, H., Alivisatos, A. P. & Liu, N. Transition from Isolated to Collective Modes in Plasmonic Oligomers. *Nano Letters* **10**, 2721-2726, (2010).

37 Oulton, R. F., Sorger, V. J., Zentgraf, T., Ma, R. M., Gladden, C., Dai, L., Bartal, G. & Zhang, X. Plasmon lasers at deep subwavelength scale. *Nature* **461**, 629-632, (2009).

38 Mayer, K. M., Hao, F., Lee, S., Nordlander, P. & Hafner, J. H. A single molecule immunoassay by localized surface plasmon resonance. *Nanotechnology* **21**, 1, (2010).

39 Haes, A. J., Hall, W. P., Chang, L., Klein, W. L. & Van Duyne, R. P. A localized surface plasmon resonance biosensor: First steps toward an assay for Alzheimer's disease. *Nano Letters* **4**, 1029-1034, (2004).

40 Novotny, L., Bian, R. X. & Xie, X. S. Theory of nanometric optical tweezers. *Phys Rev Lett* **79**, 645-648, (1997).

41 Righini, M., Zelenina, A. S., Girard, C. & Quidant, R. Parallel and selective trapping in a patterned plasmonic landscape. *Nature Physics* **3**, 477-480, (2007).

42 Grigorenko, A. N., Roberts, N. W., Dickinson, M. R. & Zhang, Y. Nanometric optical tweezers based on nanostructured substrates. *Nature Photonics* **2**, 365-370, (2008).

Reference

43 Pendry, J. B., Holden, A. J., Robbins, D. J. & Stewart, W. J. Low frequency plasmons in thin-wire structures. *J Phys-Condens Mat* **10**, 4785-4809, (1998).

44 Yen, T. J., Padilla, W. J., Fang, N., Vier, D. C., Smith, D. R., Pendry, J. B., Basov, D. N. & Zhang, X. Terahertz magnetic response from artificial materials. *Science* **303**, 1494-1496, (2004).

45 Tong, L. M., Miljkovic, V. D. & Kall, M. Alignment, Rotation, and Spinning of Single Plasmonic Nanoparticles and Nanowires Using Polarization Dependent Optical Forces. *Nano Letters* **10**, 268-273, (2010).

46 Alu, A. & Engheta, N. All Optical Metamaterial Circuit Board at the Nanoscale. *Phys Rev Lett* **103**, 143902, (2009).

47 Engheta, N., Salandrino, A. & Alu, A. Circuit elements at optical frequencies: Nanoinductors, nanocapacitors, and nanoresistors. *Phys Rev Lett* **95**, 095504, (2005).

48 Klein, M. W., Enkrich, C., Wegener, M. & Linden, S. Second-harmonic generation from magnetic metamaterials. *Science* **313**, 502-504, (2006).

49 Potton, R. J. Reciprocity in optics. *Rep Prog Phys* **67**, 717-754, (2004).

50 Wang, S., Szobota, S., Wang, Y., Volgraf, M., Liu, Z., Sun, C., Trauner, D., Isacoff, E. Y. & Zhang, X. All optical interface for parallel, remote, and spatiotemporal control of neuronal activity. *Nano Letters* **7**, 3859-3863, (2007).

51 Shimizu, K. T., Fabbri, J. D., Jelincic, J. J. & Melosh, N. A. Soft deposition of large-area metal contacts for molecular electronics. *Advanced Materials* **18**, 1499, (2006).

52 Socoliuc, A., Gnecco, E., Maier, S., Pfeiffer, O., Baratoff, A., Bennewitz, R. & Meyer, E. Atomic-scale control of friction by actuation of nanometer-sized contacts. *Science* **313**, 207-210, (2006).

53 Urbakh, M., Klafter, J., Gourdon, D. & Israelachvili, J. The nonlinear nature of friction. *Nature* **430**, 525-528, (2004).

54 Tao, A. R., Huang, J. X. & Yang, P. D. Langmuir-Blodgettry of Nanocrystals and Nanowires. *Accounts Chem Res* **41**, 1662-1673, (2008).

55 Lereu, A. L., Passian, A., Farahi, R. H., Zahrai, S. & Thundat, T. Plasmonic Marangoni forces. *J Eur Opt Soc-Rapid* **1**, 06030, (2006).

56 Chen, K. P., Drachev, V. P., Borneman, J. D., Kildishev, A. V. & Shalaev, V. M. Drude Relaxation Rate in Grained Gold Nanoantennas. *Nano Letters* **10**, 916-922, (2010).

57 Cheng, Z., Chaikin, P. M. & Mason, T. G. Light streak tracking of optically trapped thin microdisks. *Phys Rev Lett* **89**, 108303, (2002).

58 Landau, L. D. & Lifshitz, E. M. in *Mechanics* Vol. 1 (Butterworth Heinemann, 1976).

59 Husnik, M., Klein, M. W., Feth, N., Konig, M., Niegemann, J., Busch, K., Linden, S. & Wegener, M. Absolute extinction cross-section of individual magnetic split-ring resonators. *Nature Photonics* **2**, 614-617, (2008).

60 Constantinescu, V. N. *Laminar Viscous Flow*. (Springer, 1995).

61 Favero, I. & Karrai, K. Optomechanics of deformable optical cavities. *Nature Photonics* **3**, 201-205, (2009).

62 Povinelli, M. L., Loncar, M., Ibanescu, M., Smythe, E. J., Johnson, S. G., Capasso, F. & Joannopoulos, J. D. Evanescent-wave bonding between optical waveguides. *Opt Lett* **30**, 3042-3044, (2005).

63 Ng, J., Chan, C. T., Sheng, P. & Lin, Z. F. Strong optical force induced by morphology-dependent resonances. *Opt Lett* **30**, 1956-1958, (2005).

64 Li, M., Pernice, W. H. P., Xiong, C., Baehr-Jones, T., Hochberg, M. & Tang, H. X. Harnessing optical forces in integrated photonic circuits. *Nature* **456**, 480-484, (2008).

65 Kinkhabwala, A., Yu, Z. F., Fan, S. H., Avlasevich, Y., Mullen, K. & Moerner, W. E. Large single-molecule fluorescence enhancements produced by a bowtie

nanoantenna. *Nature Photonics* **3**, 654-657, (2009).

66 Liu, N., Langguth, L., Weiss, T., Kastel, J., Fleischhauer, M., Pfau, T. & Giessen, H. Plasmonic analogue of electromagnetically induced transparency at the Drude damping limit. *Nature Materials* **8**, 758-762, (2009).

67 Liu, N., Giesen, F., Belov, M., Losby, J., Moroz, J., Fraser, A. E., McKinnon, G., Clement, T. J., Sauer, V., Hiebert, W. K. & Freeman, M. R. Time-domain control of ultrahigh-frequency nanomechanical systems. *Nature Nanotechnology* **3**, 715-719, (2008).

68 Lassagne, B., Tarakanov, Y., Kinaret, J., Garcia-Sanchez, D. & Bachtold, A. Coupling Mechanics to Charge Transport in Carbon Nanotube Mechanical Resonators. *Science* **325**, 1107-1110, (2009).

69 Rittweger, E., Han, K. Y., Irvine, S. E., Eggeling, C. & Hell, S. W. STED microscopy reveals crystal colour centres with nanometric resolution. *Nature Photonics* **3**, 144-147, (2009).

70 Liu, A. S., Jones, R., Liao, L., Samara-Rubio, D., Rubin, D., Cohen, O., Nicolaescu, R. & Paniccia, M. A high-speed silicon optical modulator based on a metal-oxide-semiconductor capacitor. *Nature* **427**, 615-618, (2004).

71 Kuo, Y. H., Lee, Y. K., Ge, Y. S., Ren, S., Roth, J. E., Kamins, T. I., Miller, D. A. B. & Harris, J. S. Strong quantum-confined Stark effect in germanium quantum-well structures on silicon. *Nature* **437**, 1334-1336, (2005).

72 Liu, J., Beals, M., Pomerene, A., Bernardis, S., Sun, R., Cheng, J., Kimerling, L. C. & Michel, J. Waveguide-integrated, ultralow-energy GeSi electro-absorption modulators. *Nature Photonics* **2**, 433-437, (2008).

73 Miller, D. A. B., Chemla, D. S., Damen, T. C., Gossard, A. C., Wiegmann, W., Wood, T. H. & Burrus, C. A. Band-Edge Electroabsorption in Quantum Well Structures - the Quantum-Confined Stark-Effect. *Phys Rev Lett* **53**, 2173-2176, (1984).

74 Xu, Q., Schmidt, B., Pradhan, S. & Lipson, M. Micrometre-scale silicon electro-optic modulator. *Nature* **435**, 325-327, (2005).

75 Novoselov, K. S. Electric Field Effect in Atomically Thin Carbon Films. *Science* **306**, 666-669, (2004).

76 Avouris, P., Chen, Z. H. & Perebeinos, V. Carbon-based electronics. *Nature Nanotechnology* **2**, 605-615, (2007).

77 Geim, A. K. & Novoselov, K. S. The rise of graphene. *Nature Materials* **6**, 183-191, (2007).

78 Schwierz, F. Graphene transistors. *Nature Nanotechnology* **5**, 487-496, (2010).

79 Bonaccorso, F., Sun, Z., Hasan, T. & Ferrari, A. Graphene photonics and optoelectronics. *Nature Photonics* **4**, 611, (2010).

80 Mak, K. F., Sfeir, M. Y., Wu, Y., Lui, C. H., Misewich, J. A. & Heinz, T. F. Measurement of the Optical Conductivity of Graphene. *Phys Rev Lett* **101**, 196405, (2008).

81 Nair, R. R., Blake, P., Grigorenko, A. N., Novoselov, K. S., Booth, T. J., Stauber, T., Peres, N. M. R. & Geim, A. K. Fine Structure Constant Defines Visual Transparency of Graphene. *Science* **320**, 1308-1308, (2008).

82 Wang, F., Zhang, Y., Tian, C., Girit, C., Zettl, A., Crommie, M. & Shen, Y. R. Gate-Variable Optical Transitions in Graphene. *Science* **320**, 206-209, (2008).

83 Sun, Z. P., Popa, D., Hasan, T., Torrisi, F., Wang, F. Q., Kelleher, E. J. R., Travers, J. C., Nicolosi, V. & Ferrari, A. C. A stable, wideband tunable, near transform-limited, graphene-mode-locked, ultrafast laser. *Nano Res* **3**, 653-660, (2010).

84 Xia, F. N., Mueller, T., Lin, Y. M., Valdes-Garcia, A. & Avouris, P. Ultrafast graphene photodetector. *Nature Nanotechnology* **4**, 839-843, (2009).

85 Mueller, T., Xia, F. N. A. & Avouris, P. Graphene photodetectors for high-speed optical communications. *Nature Photonics* **4**, 297-301, (2010).

86 Lin, Y. M., Dimitrakopoulos, C., Jenkins, K. A., Farmer, D. B., Chiu, H. Y., Grill, A. & Avouris, P. 100-GHz Transistors from Wafer-Scale Epitaxial Graphene.

Science **327**, 662-662, (2010).

87 Liao, L., Lin, Y. C., Bao, M. Q., Cheng, R., Bai, J. W., Liu, Y. A., Qu, Y. Q., Wang, K. L., Huang, Y. & Duan, X. F. High-speed graphene transistors with a self-aligned nanowire gate. *Nature* **467**, 305-308, (2010).

88 Bolotin, K. I., Sikes, K. J., Jiang, Z., Klima, M., Fudenberg, G., Hone, J., Kim, P. & Stormer, H. L. Ultrahigh electron mobility in suspended graphene. *Solid State Communications* **146**, 351-355, (2008).

89 Du, X., Skachko, I., Barker, A. & Andrei, E. Y. Approaching ballistic transport in suspended graphene. *Nature Nanotechnology* **3**, 491-495, (2008).

90 Kampfrath, T., Perfetti, L., Schapper, F., Frischkorn, C. & Wolf, M. Strongly coupled optical phonons in the ultrafast dynamics of the electronic energy and current relaxation in graphite. *Phys Rev Lett* **95**, 187403, (2005).

91 Zhang, Y. B., Brar, V. W., Girit, C., Zettl, A. & Crommie, M. F. Origin of spatial charge inhomogeneity in graphene. *Nature Physics* **5**, 722-726, (2009).

92 Zhou, S. Y., Gweon, G. H., Fedorov, A. V., First, P. N., De Heer, W. A., Lee, D. H., Guinea, F., Neto, A. H. C. & Lanzara, A. Substrate-induced bandgap opening in epitaxial graphene. *Nature Materials* **6**, 770-775, (2007).

93 Zhou, S. Y., Gweon, G. H., Graf, J., Fedorov, A. V., Spataru, C. D., Diehl, R. D., Kopelevich, Y., Lee, D. H., Louie, S. G. & Lanzara, A. First direct observation of Dirac fermions in graphite. *Nature Physics* **2**, 595-599, (2006).

94 Rogers, J. A., Someya, T. & Huang, Y. G. Materials and Mechanics for Stretchable Electronics. *Science* **327**, 1603-1607, (2010).

95 Kim, K. S., Zhao, Y., Jang, H., Lee, S. Y., Kim, J. M., Kim, K. S., Ahn, J.-H., Kim, P., Choi, J.-Y. & Hong, B. H. Large-scale pattern growth of graphene films for stretchable transparent electrodes. *Nature* **457**, 706-710, (2009).

Chapter 1 Introduction